Multidimensional coherent spectroscopy of light-driven states and their collective modes in multiband superconductors

Martin Mootz[1], Liang Luo[1], Chuankun Huang,[1,2] Jigang Wang,[1,2] and llias E. Perakis[3]

[1]*Ames National Laboratory, U.S. Department of Energy, Ames, Iowa 50011, USA*
[2]*Department of Physics and Astronomy, Iowa State University, Ames, Iowa 50011, USA*
[3]*Department of Physics, University of Alabama at Birmingham, Birmingham, Alabama 35294-1170, USA*

We present a comprehensive theory of light-controlled multiband superconductivity, and apply it to predict distinctive signatures of light-driven superconducting (SC) states in terahertz multidimensional coherent spectroscopy (THz-MDCS) experiments. We first derive gauge-invariant Maxwell-Bloch equations for multiband BCS superconductors with spatial fluctuations. We consider driving electromagnetic fields determined self-consistently by Maxwell's equations. By calculating the THz-MDCS spectra measured experimentally in the clean SC limit, we identify unique signatures of finite-momentum Cooper-pairing states that live longer than the laser pulse. They are controlled by a pair of THz laser pulses with well-defined relative phase (pulse pair). The pseudospin oscillators that describe the properties of these SC states are parametrically driven by both finite-momentum Cooper pairing and by time oscillations of the order-parameter relative phase. We show that such strong parametric driving leads to drastic changes in the THz-MDCS spectral shape from the predictions of third-order nonlinear susceptibility calculations. These spectral changes strongly depend on the interband-to-intraband interaction ratio and on the collective modes of the light-driven state. For negligible interband interaction, the spectra show a transition with increasing field, from traditional pump-probe, four-wave-mixing, and third-harmonic generation peaks determined by the laser frequency to sidebands determined by the excitations of the driven system. These sidebands emerge from difference-frequency Raman processes in the nonequilibrium SC state. For interband couplings weaker than the intraband pairing, we show that the Leggett phase collective mode leads to harmonic sidebands around the traditional pump-probe peaks. Additional Higgs collective mode peaks result from light-induced inversion-symmetry breaking in a thin-film geometry. For strong interband coupling, we find a transition from a nonequilibrium finite Cooper-pair momentum state characterized by hybrid-Higgs amplitude mode peaks in THz-MDCS spectra to a driven state identified experimentally by the emergence of Floquet-type sidebands at bi-Higgs frequencies. Those dominant bi-Higgs-frequency satellites are manifestations of a new order parameter relative phase collective mode that characterizes the nonequilibrium SC state. The predicted interaction- and field-dependent transitions in the spectral profile allow us to propose THz-MDCS experiments for quantum tomography of light-driven superconductivity.

DOI: 10.1103/PhysRevB.109.014515

I. INTRODUCTION

Terahertz multidimensional coherent spectroscopy (THz-MDCS) is developing into an important tool for unraveling the dynamics of electronic and vibrational excitations of matter. In the past, such multidimensional spectroscopy has been used in conventional materials to investigate electronic excitations [1–5], spin waves [6,7], and vibrational modes [8,9], among others. In superconducting (SC) systems, however, THz-MDCS experiments and corresponding theories have been rare so far [10–13]. As a result, it is not yet clear how to obtain new information about nonequilibrium superconductivity and other outstanding questions by analyzing THz-MDCS data. The SC dipole-forbidden collective modes, which characterize the unique properties of superconductivity, overlap in energy with the quasiparticle continuum. In multiband superconductors, the collective mode properties depend on the ratio of interband over intraband interaction strength, as well as on the driving light field. So far, the

THz-driven dynamics of superconductors has been mostly studied with traditional single-particle pump-probe spectroscopies [14–19]. These experiments have been interpreted by using nonlinear susceptibility expansions [20–23], Anderson pseudospin models [10,24–28], or Green's functions [29–31], in the clean SC limit or including disorder effects [32–34]. In our previous works, we have shown that THz light-wave acceleration of the Cooper-pair condensate gives access to long-lived SC states with finite-momentum pairing. These states are witnessed experimentally, e.g., by the emergence above critical driving field of spectral peaks centered at frequencies forbidden by the equilibrium symmetry. They range from quasiparticle quantum states, accessed by single-cycle THz pulses [35], to gapless-SC states with finite coherence and broken inversion symmetry, accessed by multicycle THz pulses [36]. Full characterization of the different nonequilibrium states requires detection of the collective modes [37] of the underlying order parameters. Typical collective excitations of multiband superconductors include amplitude oscillations

of the SC order parameter (Higgs mode) and oscillations of the relative phase of the SC order parameters in different bands (Leggett mode) [21,25]. In addition to identifying how their collective modes differ from those of the equilibrium SC state, full characterization of strongly driven SC states also requires the resolution of high-order correlations that go beyond the traditional third-order nonlinear responses known to dominate close to equilibrium [10,11]. Examples of such high-order correlations in light-driven SC states include sideband generation at bi-Higgs frequencies analogous to Floquet sidebands [11] and correlated wave-mixing peaks in THz-MDCS [10].

More generally, understanding the properties of quantum materials for, e.g., quantum science applications, requires experiments that can measure and control correlation between different elementary excitations, like THz-MDCS. Quantum tomography of THz-driven condensate states is, however, challenging. Unlike in semiconductors, collective modes of SC states do not couple linearly to the electromagnetic fields without a finite Cooper-pair momentum [28,38–44]. In addition, the SC energy gap is quenched coherently via Raman processes during cycles of THz light-wave oscillations [10]. Finally, the dynamics of the phase of the complex order parameter must be considered. The interpretation of the experimental spectra is further complicated by the multiple excitation pathways contributing to the same nonlinear signals [32,45]. Recent simulations of THz-MDCS experiments proposed the possibility for ultrafast visualization and quantum control of THz-driven SC states [10]. Resolution of high-order correlation and relative-phase collective modes has been recently realized by THz-MDCS experimental studies of an iron-based superconductor [11]. Such THz-MDCS experiments allow the identification of high-order nonlinear responses through the observation of new peaks centered at high frequencies. These peaks are distinguished in two-dimensional frequency space from the conventional pump-probe peaks accessed through traditional one-dimensional pump-probe spectroscopies.

In this paper, we present a comprehensive theory of THz-MDCS experiments on multiband BCS superconductors, and apply it to identify unique experimental signatures of light-driven superconductivity. By extending the density matrix approach of Ref. [10] to the case of multiple coupled bands, we derive self-consistent, gauge-invariant SC Bloch equations (Appendix B). Together with Maxwell's wave equation, these SC Bloch equations allow us to propose distinctive experimental signatures of parametrically driven SC states. For this purpose, we consider the phase-locked, collinear two-pulse geometry of Fig. 1(a). Two THz pulses with equal strength and spectral profile, and with well-defined relative phase (phase-locked pulse pair), excite a SC thin film. These two pulses are separated by the interpulse time delay τ that controls their phase difference. We study the pulse-pair excitation of a three-pocket band structure model, with a hole (h) pocket centered at the Γ point and two electron (e) pockets located at $(\pi, 0)$ and $(0, \pi)$ [Fig. 1(b)]. The corresponding SC order-parameter components in the different bands are denoted as Δ_λ, with $\lambda = $ e, h. In this paper we consider the case of a homogeneous system and approximate the spatial fluctuations in the full equations of motion presented in Appendix B,
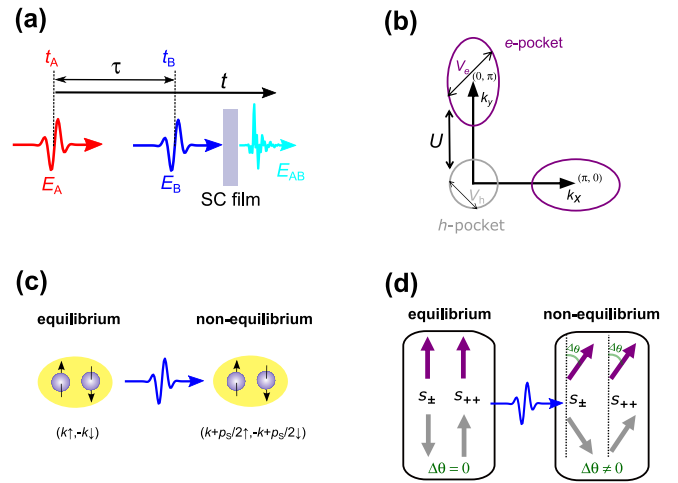

FIG. 1. Multidimensional coherent spectroscopy of multiband superconductors. (a) Schematic representation of the two-dimensional terahertz (THz) configuration considered in this paper. A superconducting (SC) thin film is excited by a pulse pair consisting of two collinear, phase-locked THz pulses of similar strength and spectrum. Pulse E_A (red) is centered at $t_A = 0$, while pulse E_B (blue) is centered at $t_B = \tau$. The interpulse delay $\tau = t_B - t_A$ controls their relative phase. $E_{AB}(t, \tau)$ (cyan) is the transmitted electric field after excitation by both pulses. The experimentally measured signal, $E_{NL} = E_{AB} - E_A - E_B$, vanishes in the absence of correlations between excitations driven by different pulses, which distinguishes THz-MDCS from the SC nonlinear response to a single pulse and from conductivity measurements. (b) Three-pocket band structure model used in the simulations. A hole (h) pocket is centered at the Γ point and two electron (e) pockets are located at $(\pi, 0)$ and $(0, \pi)$ in **k** space. We consider intraband pairing interactions V_e and V_h and interband coupling U between the electron and hole pockets. Two effects determine the nonequilibrium SC state. (c) The effective field inside the SC thin film accelerates the condensate and induces a finite Cooper-pair center-of-mass momentum $\mathbf{p}_S$ that persists after the pulse. This THz light-wave acceleration results in a long-lived, finite-momentum Cooper-pairing state $(\mathbf{k} + \mathbf{p}_S/2 \uparrow, -\mathbf{k} + \mathbf{p}_S/2 \downarrow)$. (d) Parametric driving of the superconductor by the dynamics of the order-parameter relative phase. Left box: $s_\pm$ (s_{++}) order-parameter symmetry with $\Delta\theta = 0$ gives a pseudomagnetic field (24) with x-axis components pointing in opposite (same) directions in different bands. Pseudospins orient along this pseudomagnetic field in equilibrium. Right box: light-induced nonequilibrium state with long-lived relative phase $\Delta\theta(t) \neq 0$ above critical pulse-pair excitation is determined by a pseudomagnetic field (24) whose $x - y$ components depend on $\Delta\theta(t)$.

by assuming that their characteristic length (e.g., the mean-free path) exceeds the coherence length that characterizes the size of the Cooper pair. The SC state can then be described by introducing Anderson pseudospins located at different momentum points **k** [37]. In this representation, up (down) pseudospins describe filled (empty) $(\mathbf{k} \uparrow, -\mathbf{k} \downarrow)$ Cooper-pair states. Canted pseudospins describe the superposition of up and down states on the Bloch sphere. This canting depends on the SC order parameter, which determines the direction of the pseudomagnetic field that describes the pseudospin orientation. For example, for a multiband superconductor with $s_\pm$ (s_{++}) order-parameter symmetry, a phase difference of π (0)

leads to opposite (same) signs between the order parameters of the electron and hole pockets [Fig. 1(d), left box], which fixes the corresponding pseudomagnetic field and pseudospin components in equilibrium. This order-parameter relative phase depends on the ratio between interband and intraband interaction strengths. Here we consider the effects of the intraband SC pairing interactions $V_{e,h}$ and interband Coulomb-induced coupling U between electron and hole pockets on the THz-MDCS spectral profiles. We show that the relative strength of interband vs intraband interactions plays a critical role in determining this spectral profile, as well as how this profile changes with increasing driving field. In this way, the THz-MDCS spectral peaks provide direct evidence about the properties of the SC state and how the latter evolves with increasing THz field driving.

We wish to highlight the importance of two competing effects for inducing controllable transitions between different light-driven SC states in multiband SCs. First is SC driving by a finite center-of-mass Cooper-pair momentum ($\mathbf{p}_S$) driven by the laser field. Our results demonstrate that the effective local field that accelerates the SC condensate into a finite $\mathbf{p}_S$ state is modified from the external THz laser field by electromagnetic wave propagation in a thin-film geometry. We show that this modified effective driving field leads to a finite center-of-mass Cooper-pair momentum state that can persist well after the pulse. In particular, the moving condensate momentum $\mathbf{p}_S(t)$ decays slowly in time for a thin-film geometry due to radiative damping [28]. This persistent condensate motion results in $(\mathbf{k} + \mathbf{p}_S/2 \uparrow, -\mathbf{k} + \mathbf{p}_S/2 \downarrow)$ Cooper pairs, i.e., to finite-momentum pairing [Fig. 1(c)], controlled by the THz field. As a result of a light-induced DC component of $\mathbf{p}_S$, the equilibrium inversion symmetry is broken dynamically. This prediction was verified experimentally by the observation of high-harmonic generation peaks centered at equilibrium-forbidden frequencies [36,46]. Hybrid Higgs collective modes also become observable then. They give rise to distinct peaks in the THz-MDCS spectra, located at the symmetry-forbidden Higgs mode frequency, even in the clean system. These Higgs spectral peaks emerge with increasing light-field strength [11]. Second, THz excitation of the SC system yields time-dependent deviations from equilibrium of the relative phase of the order-parameter components between electron and hole pockets, $\Delta\theta(t)$. The latter leads to a change of the pseudomagnetic field [Fig. 1(d), right box] from its equilibrium orientation along the x direction [Fig. 1(d), left box]. For weak interband coupling U, the relative phase dynamics is known to describe a Leggett collective mode located within the excitation energy gap. We show that, in this case, the THz-MDCS spectra display strong Leggett mode sidebands around the conventional pump-probe signals. This Leggett mode, however, moves within the quasiparticle continuum when the interband interaction exceeds the intraband interaction, as in iron-based superconductors. Therefore, the Leggett mode becomes strongly damped with increasing U, which diminishes its contribution to the dynamics. However, we will demonstrate below that, above critical THz driving, the photoexcitation leads to undamped oscillations of $\Delta\theta$ at the Higgs frequency, i.e., at the same frequency as the amplitude oscillations. We will show that, with strong interband interaction, the nonlinear coupling between pseudospin and

relative phase oscillations at the Higgs frequency manifests itself in Floquet-type sidebands located at twice the Higgs frequency.

The paper is organized as follows. In Sec. II we summarize the self-consistent gauge-invariant SC Bloch equations for multiband superconductors. These equations of motion, derived in detail in Appendix B, present the basis for our simulations. In Sec. III we describe the excitations of the nonequilibrium SC state predicted by these equations in the homogeneous limit. In particular, we discuss the role of the competition between finite condensate momentum and long-lived relative phase oscillations. We first apply our theory in Sec. IV to calculate the THz-MDCS signals for multiband superconductors by neglecting the electromagnetic propagation effects. In this case, the Cooper-pair momentum vanishes after the pulse, similar to previous calculations. We discuss the THz-MDCS spectral shape for vanishing interband interaction in Sec. IV A. These results extend the results of Ref. [10], obtained for strong narrow-band pump and weak broadband probe pulses, to the case of strong pulse-pair excitation. The THz-MDCS spectral profiles for weak and strong interband coupling U are discussed in Sec. IV B. Then we show in Sec. V how the above-obtained results change drastically when the effects of electromagnetic pulse propagation in a thin-film geometry are included in our calculation. In Sec. V A we present the results with such dynamical inversion-symmetry breaking for small interband coupling strength. In Sec. V B we show how that THz-MDCS spectral profile changes drastically when the interband coupling exceeds the intraband pairing strength with persisting finite-momentum pairing. We end with our summary in Sec. VI. In the Appendixes, we present the general gauge-invariant equations that include the effects of spatial fluctuations and show the equivalence of the equations of motion to the conventional pseudospin model in the case of homogeneous SC systems and excitation conditions. We also identify the different nonlinear processes that determine the overall spectral profile of THz-MDCS depending on the pulse-pair excitation conditions.

II. GAUGE-INVARIANT DESCRIPTION OF THZ-MDCS IN MULTIBAND SUPERCONDUCTORS

A. Bogoliubov–de Gennes Hamiltonian

We model spatially dependent superconductors by using the Bogoliubov–de Gennes Hamiltonian [29,31]

$$
\begin{aligned}
H = \sum_{\nu,\alpha} \int \mathrm{d}^3\mathbf{x}\, \psi_{\alpha,\nu}^\dagger(\mathbf{x}) \big\{ & \xi_\nu[\mathbf{p} - e\mathbf{A}(\mathbf{x},t)] \\
& + e\phi(\mathbf{x},t) + \mu_{\mathrm{H}}^\nu(\mathbf{x}) + \mu_{\mathrm{F}}^{\alpha,\nu}(\mathbf{x}) \big\} \psi_{\alpha,\nu}(\mathbf{x}) \\
& - \sum_\nu \int \mathrm{d}^3\mathbf{x}[\Delta_\nu(\mathbf{x})\psi_{\uparrow,\nu}^\dagger(\mathbf{x})\psi_{\downarrow,\nu}^\dagger(\mathbf{x}) + \mathrm{H.c.}],
\end{aligned} \quad (1)
$$

which is explicitly derived in Appendix A by factorizing the full interacting Hamiltonian as in Refs. [37,47]. The fermionic field operators $\psi_{\alpha,\nu}^\dagger(\mathbf{x})$ and $\psi_{\alpha,\nu}(\mathbf{x})$ create and annihilate an electron in states labeled by the spin index α and the hole ($\nu = \mathrm{h}$) or electron ($\nu = \mathrm{e}$) pocket index. The band dispersions give the kinetic energy contributions $\xi_\nu[\mathbf{p} - e\mathbf{A}(\mathbf{x},t)]$,

which depend on the electron momentum operator $\mathbf{p} = -i\nabla_{\mathbf{x}}$ ($\hbar = 1$), the vector potential $\mathbf{A}(\mathbf{x}, t)$, and the electron charge $-e$. The scalar potential is denoted by $\phi(\mathbf{x}, t)$. In the case of disordered SCs, we must add the impurity potential. The SC order-parameter components at different pockets ν are given by

$$\Delta_\nu(\mathbf{x}) = -\sum_\lambda g_{\nu,\lambda}\langle\psi_{\downarrow,\lambda}(\mathbf{x})\psi_{\uparrow,\lambda}(\mathbf{x})\rangle = |\Delta_\nu(\mathbf{x})|e^{-i\theta_\nu(\mathbf{x})}, \quad (2)$$

where $\theta_\nu(\mathbf{x})$ are the corresponding phases and $g_{\lambda,\nu}$ describe the interband ($\lambda \neq \nu$) and intraband ($\lambda = \nu$) interactions. In Eq. (1), we have added the Hartree and Fock contributions. The Hartree contribution is given by

$$\mu_H^\nu(\mathbf{x}) = \sum_\sigma \int d^3\mathbf{x}' V(\mathbf{x} - \mathbf{x}')n_{\sigma,\nu}(\mathbf{x}'),$$

$$n_{\sigma,\nu}(\mathbf{x}) = \langle\psi_{\sigma,\nu}^\dagger(\mathbf{x})\psi_{\sigma,\nu}(\mathbf{x})\rangle, \quad (3)$$

where $V(\mathbf{x})$ is the Coulomb potential with Fourier transformation $V_\mathbf{q} = e^2/(\varepsilon_0 q^2)$. This contribution moves the Nambu-Goldstone phase mode of the SC order parameters to the plasma energy (Anderson-Higgs mechanism) [37]. The Fock contribution is given by

$$\mu_F^{\alpha,\nu}(\mathbf{x}) = -g_{\nu,\nu}n_{\alpha,\nu}(\mathbf{x}). \quad (4)$$

Its main role is that it ensures charge conservation.

B. Gauge-invariant SC Bloch equations

To calculate the THz-MDCS spectra, we first model the THz-driven SC quantum dynamics by extending the density matrix approach of Ref. [28] to the multiband case. In particular, we derive spatially dependent gauge-invariant SC Bloch equations for the Wigner function $\tilde{\rho}^{(\nu)}(\mathbf{k}, \mathbf{R})$, which, in addition to the Cooper-pair relative momentum $\mathbf{k}$, depends on the center-of-mass coordinate $\mathbf{R}$. The full spatially dependent Bloch equations are presented in Appendix B. Here we present the results for the THz-MDCS spectra profile for sufficiently weak spatial $\mathbf{R}$ dependence, such that we can omit all orders of $O(\nabla_\mathbf{k} \cdot \nabla_\mathbf{R})$ in the gradient expansion of the full spatially dependent SC Bloch equations (B5)–(B7). We also assume homogeneous E fields. Since the contribution of the Hartree potential to the nonlinear response is negligible in the case of weak spatial dependence, we can neglect μ_H^ν, but must keep the Fock energy $\mu_F^\nu(t)$ to ensure charge conservation during laser excitation.

To make the connection with previous theoretical approaches used to describe the SC quantum dynamics, we express the gauge-invariant density matrix in terms of Anderson pseudospin components at each wave vector $\mathbf{k}$:

$$\tilde{\rho}^{(\nu)}(\mathbf{k}) = \sum_{n=0}^3 \tilde{\rho}_n^{(\nu)}(\mathbf{k})\sigma_n, \quad (5)$$

where $\sigma_n, n = 1\ldots3$, are the Pauli spin matrices, σ_0 is the unit matrix, $\tilde{\rho}_n^{(\nu)}(\mathbf{k}), n = 1, \ldots, 3$, are the pseudospin components in band ν at momentum $\mathbf{k}$, and $\tilde{\rho}_0^{(\nu)}(\mathbf{k})$ describes the total charge. By retaining only the lowest term in the gradient expansion of the spatially dependent equations derived in Appendix B, we obtain the following gauge-invariant SC

Bloch equations describing a homogeneous system:

$$\frac{\partial}{\partial t}\tilde{\rho}_0^{(\nu)}(\mathbf{k}) = -e\,\mathbf{E}(t)\cdot\nabla_\mathbf{k}\tilde{\rho}_3^{(\nu)}(\mathbf{k})$$
$$-|\Delta_\nu|\big[\sin\delta\theta_\nu\big[\tilde{\rho}_1^{(\nu)}(\mathbf{k}_-) - \tilde{\rho}_1^{(\nu)}(\mathbf{k}_+)\big]$$
$$+\cos\delta\theta_\nu\big[\tilde{\rho}_2^{(\nu)}(\mathbf{k}_-) - \tilde{\rho}_2^{(\nu)}(\mathbf{k}_+)\big]\big],$$

$$\frac{\partial}{\partial t}\tilde{\rho}_1^{(\nu)}(\mathbf{k}) = -E_\nu(\mathbf{k})\tilde{\rho}_2^{(\nu)}(\mathbf{k}) - |\Delta_\nu|\sin\delta\theta_\nu N_\nu(\mathbf{k}),$$

$$\frac{\partial}{\partial t}\tilde{\rho}_2^{(\nu)}(\mathbf{k}) = E_\nu(\mathbf{k})\tilde{\rho}_1^{(\nu)}(\mathbf{k}) - |\Delta_\nu|\cos\delta\theta_\nu N_\nu(\mathbf{k}),$$

$$\frac{\partial}{\partial t}\tilde{\rho}_3^{(\nu)}(\mathbf{k}) = -e\,\mathbf{E}(t)\cdot\nabla_\mathbf{k}\tilde{\rho}_0^{(\nu)}(\mathbf{k})$$
$$-|\Delta_\nu|\big[\sin\delta\theta_\nu\big[\tilde{\rho}_1^{(\nu)}(\mathbf{k}_-) + \tilde{\rho}_1^{(\nu)}(\mathbf{k}_+)\big]$$
$$+\cos\delta\theta_\nu\big[\tilde{\rho}_2^{(\nu)}(\mathbf{k}_+) + \tilde{\rho}_2^{(\nu)}(\mathbf{k}_-)\big]\big], \quad (6)$$

where $\mathbf{k}_\pm = \mathbf{k} \pm \mathbf{p}_S/2$. In the above equations, we introduced the phase-space filling contribution

$$N_\nu(\mathbf{k}) = \tilde{\rho}_0^{(\nu)}(\mathbf{k}_-) - \tilde{\rho}_3^{(\nu)}(\mathbf{k}_-) - \tilde{\rho}_0^{(\nu)}(\mathbf{k}_+) - \tilde{\rho}_3^{(\nu)}(\mathbf{k}_+), \quad (7)$$

and the time- and band-dependent energy

$$E_\nu(\mathbf{k}) = \xi_\nu(\mathbf{k}_-) + \xi_\nu(\mathbf{k}_+) + 2\big(\mu_{\text{eff}} + \mu_F^\nu\big), \quad (8)$$

where $\mu_{\text{eff}}(t) = e\phi(\mathbf{x}, t) + \frac{1}{2}\frac{d}{dt}\theta_{\nu_0}$ is the effective chemical potential with time-dependent contributions from the phase dynamics and any scalar potential. The Fock energy modifies this effective time-dependent chemical potential to ensure charge conservation at all times:

$$\mu_F^\nu \equiv \frac{1}{2}\big(\mu_F^{\downarrow,\nu} + \mu_F^{\uparrow,\nu}\big) = -g_{\nu,\nu}\sum_\mathbf{k}\big[1 + \tilde{\rho}_3^{(\nu)}(\mathbf{k})\big]. \quad (9)$$

The order-parameter amplitude

$$|\Delta_\nu| = -e^{-i\delta\theta_\nu}\sum_{\lambda,\mathbf{k}}g_{\nu,\lambda}\big[\tilde{\rho}_1^{(\lambda)}(\mathbf{k}) - i\tilde{\rho}_2^{(\lambda)}(\mathbf{k})\big]$$
$$= -\sum_{\lambda,\mathbf{k}}g_{\nu,\lambda}\big[\cos\delta\theta_\nu\tilde{\rho}_1^{(\lambda)}(\mathbf{k}) - \sin\delta\theta_\nu\tilde{\rho}_2^{(\lambda)}(\mathbf{k})\big] \quad (10)$$

remains real valued in the numerical calculation at all times and fields. The above equations in the homogeneous limit provide a starting point to add weak disorder effects through a Born approximation treatment of the impurity potential. Disorder effects will enhance the collective mode contributions predicted here to result from a persisting inversion-symmetry breaking controlled by light. In the case of strong spatial fluctuations (e.g., dirty limit SC), a more appropriate starting point is the equations of motion for $\tilde{\rho}^{(\nu)}(\mathbf{r}, \mathbf{R})$ obtained from Eqs. (B17)–(B19) by Fourier transform.

The SC Bloch equations (6) include four different dynamical sources that drive the Anderson pseudospins: (i) The light-induced condensate center-of-mass momentum $\mathbf{p}_S$ differs from the laser vector potential $\mathbf{A}(t)$ considered in previous works due to electromagnetic propagation effects. In addition to its oscillatory contribution during photoexcitation, it also exhibits a static component, which is generated by difference-frequency Raman processes [10]. This DC momentum remains finite after the pulse and decays slowly in time, leading to a nonequilibrium condensate state with

finite-momentum Cooper pairing [Fig. 1(c)]. (ii) The effective chemical potential $\mu_{\text{eff}}(t)$, whose time dependence is determined by the nonequilibrium order-parameter phase in reference band ν_0:

$$\frac{d\theta_{\nu_0}}{dt} = -2\,e\,\phi + \frac{1}{|\Delta_{\nu_0}|} \sum_{\nu,\mathbf{k}} g_{\nu_0,\nu}\big[\xi_\nu(\mathbf{k}_-) + \xi_\nu(\mathbf{k}_+) + 2\mu_F^\nu\big]$$
$$\times \tilde{\rho}_1^{(\nu)}(\mathbf{k}) + \frac{1}{|\Delta_{\nu_0}|} \sum_{\nu,\mathbf{k}} g_{\nu_0,\nu}|\Delta_\nu|N_\nu(\mathbf{k})\cos(\delta\theta_\nu)\,.$$

(11)

(iii) The time-dependent phase difference of the order parameters in different bands ν, $\delta\theta_\nu = \theta_{\nu_0} - \theta_\nu$, is given by the equation of motion

$$\frac{d\delta\theta_\nu}{dt} = \frac{1}{|\Delta_\nu|} \sum_{\lambda,\mathbf{k}} g_{\nu,\lambda}\Big[\big[\xi_\nu(\mathbf{k}_-) + \xi_\nu(\mathbf{k}_+) + 2\mu_F^\nu\big]$$
$$\times \big(\cos\delta\theta_\nu\,\tilde{\rho}_1^{(\lambda)}(\mathbf{k}) - \sin\delta\theta_\nu\,\tilde{\rho}_2^{(\lambda)}(\mathbf{k})\big)$$
$$- |\Delta_\lambda|N_\nu(\mathbf{k})\cos(\delta\theta_\nu - \delta\theta_\lambda)\Big]\,.$$

(12)

This relative phase dynamics follows from the constraint imposed by the gauge invariance,

$$\sum_{\lambda,\mathbf{k}} g_{\nu,\lambda}\big[\sin\delta\theta_\nu\,\tilde{\rho}_1^{(\lambda)}(\mathbf{k}) + \cos\delta\theta_\nu\,\tilde{\rho}_2^{(\lambda)}(\mathbf{k})\big] = 0.$$

(13)

This constraint is satisfied exactly at all times and for any strong driving field. (iv) The order-parameter amplitudes $|\Delta_\nu(t)|$ in each band, which are coherently quenched during cycles of THz light-field oscillations via difference-frequency Raman processes [10].

To model the THz-MDCS spectra measured in the experiments, we express the gauge-invariant supercurrent density in terms of $\tilde{\rho}_0^{(\lambda)}(\mathbf{k})$ as

$$J(t) = \frac{2e}{V} \sum_{\mathbf{k},\lambda} \boldsymbol{\nabla}_\mathbf{k}\xi_\lambda(\mathbf{k})\tilde{\rho}_0^{(\lambda)}(\mathbf{k}),$$

(14)

with normalization volume V. The measured nonlinear differential transmission follows from the transmitted electric field obtained by solving Maxwell's equations as described in Ref. [28]. For a thin-film geometry, we can neglect the spatial dependence, so the effective field becomes

$$E(t) = E_{\text{THz}}(t) - \frac{\mu_0\,c\,d}{2n}J(t).$$

(15)

Here, $E_{\text{THz}}(t)$ corresponds to the applied THz laser electric field, while n denotes the refractive index of the SC system, d is the thickness of the SC thin film, and c is the speed of light. The dynamics of the current density (14) in linear response can be described by the London equation $\partial J(t)/\partial t = n_s e^2/mE(t)$, where n_s is the superfluid density. Using Eq. (15), one obtains

$$\frac{\partial J(t)}{\partial t} = \frac{n_s e^2}{m}E_{\text{THz}}(t) - \frac{J(t)}{\tau}.$$

(16)

The current density decays due to radiative damping with lifetime

$$\tau = \frac{2nm}{\mu_0 c n_s e^2 d},$$

(17)

where

$$n_s = \frac{4m}{\hbar^2 V} \sum_{\nu,\mathbf{k}} \boldsymbol{\nabla}_\mathbf{k}\xi_\nu(\mathbf{k}) \cdot \boldsymbol{\nabla}_\mathbf{k}\tilde{\rho}_3^{(\nu),0}(\mathbf{k})$$

(18)

is superfluid density and $\tilde{\rho}_3^{(\nu),0}(\mathbf{k})$ is the equilibrium z component of the pseudospin.

Following Refs. [10,28], the correlated signal measured in THz-MDCS experiments is given by

$$E_{\text{NL}}(t,\tau) = E_{\text{AB}}(t,\tau) - E_{\text{A}}(t) - E_{\text{B}}(t,\tau).$$

(19)

This expression applies to the case of the collinear two-pulse geometry considered in this paper [Fig. 1(a)]. Here, $E_{\text{AB}}(t,\tau)$ is the transmitted E field induced by *both* pulses A and B, which depends on both the real time t and the delay time between the two pulses τ. $E_{\text{A}}(t)$ [$E_{\text{B}}(t,\tau)$] is the transmitted electric field induced by pulse A (B). The THz-MDCS spectra are obtained by Fourier transform of $E_{\text{NL}}(t,\tau)$ with respect to both t (frequency ω_t) and τ (frequency ω_τ). Equation (15) also provides the driving field of the SC Bloch equations (6), whose solution determines the current density according to Eq. (14). The dependence of the driving field on the current density leads to a *self-consistent calculation*, whose results differ from the calculation with driving field given by the two laser pulses.

In this paper, we solve the full Bloch equations (6) for a three-pocket model band structure, which includes a hole (h) pocket centered at the Γ point and two electron (e) pockets located at $(\pi, 0)$ and $(0, \pi)$ [Fig. 1(b)]. We include interpocket e-h couplings between the hole and the two electron pockets ($g_{\text{e,h}} = g_{\text{h,e}}$), as well as intrapocket pairing interactions ($V_\lambda = g_{\lambda,\lambda}$, $\lambda = $ e, h). We neglect the interelectron pocket interactions for simplicity and calculate the THz-MDCS spectra as a function of the interband-to-intraband interaction ratio $U = g_{\text{e,h}}/V_{\text{h}}$. The electron and hole band energies are described by using the square-lattice nearest-neighbor tight-binding dispersion $\xi_\nu(\mathbf{k}) = -2\,[J_{\nu,x}\cos(k_x a) + J_{\nu,y}\cos(k_y a)] + \mu_\nu$, with hopping parameters $J_{\nu,i}$, band offset μ_ν, and lattice constant a. We choose a circular hole pocket with $J_{h,x} = J_{h,y} = 25.0$ meV and $\mu_{\text{h}} = -15.0$ meV. We introduce a particle-hole asymmetry between electron and hole pockets [43,48,49] by considering elliptical electron pockets with $J_{e,x} = -25.0$ meV, $J_{e,y} = -50.0$ meV, and $\mu_e = 15.0$ meV. Such asymmetry strongly suppresses the higher-band Higgs mode in our calculated spectra, as discussed in Ref. [18]. As lattice constant we choose $a = 4.0$ Å while we consider a sample thickness of $d = 20$ nm which is a typical thickness of superconductor thin films used in THz spectroscopy experiments [36]. We assume equilibrium SC order parameters $\Delta_{\text{h}} = 4.1$ meV for the hole pocket and $\Delta_{\text{e}} = 8.2$ meV for the electron pockets. We consider an excitation protocol where the multiband SC system is excited by a pulse pair consisting of two equal few-cycle broadband pulses with well-defined relative phase controlled by the time delay τ and central laser frequency $\omega_0 = 1$ THz. The two

electric fields used in the calculation are $\mathbf{E}_A(t')\sin(\omega_A t')$ and $\mathbf{E}_B(t')\sin(\omega_B t')$ with Gaussian envelope functions $\mathbf{E}_{A,B}(t')$. Similar to previous studies in semiconductors [1–3,50], we introduced "time vectors" $t' = (t, \tau)$ and "frequency vectors" (ω_t, ω_τ). The frequency vectors of the two pulses A and B are then $\omega_A = (\omega_0, 0)$ and $\omega_B = (\omega_0, -\omega_0)$.

III. EXCITATIONS OF THE DRIVEN SUPERCONDUCTOR

Prior to presenting our numerical results, we first identify the main drivers of nonlinearity that determine the most striking features of the THz-MDCS spectra of SCs. For this purpose, we extract from the full SC Bloch equations *pseudospin nonlinear coupled oscillator* equations of motion, obtained by extending Anderson's random phase approximation treatment of pseudospin flips and Higgs collective modes [37] to multiband SCs without linearization. We characterize the nonequilibrium state by the density matrix $\tilde{\rho}^{(\nu)}(\mathbf{k})$, which we decompose as

$$\tilde{\rho}^{(\nu)}(\mathbf{k}) = \tilde{\rho}^{(\nu),0}(\mathbf{k}) + \Delta\tilde{\rho}^{(\nu)}(\mathbf{k}), \qquad (20)$$

where $\tilde{\rho}^{(\nu),0}(\mathbf{k})$ denotes the density matrix of the thermal state, where $\partial_t\tilde{\rho}^{(\nu),0}(\mathbf{k}) = 0$, and $\Delta\tilde{\rho}^{(\nu)}(\mathbf{k})$ describes the full nonthermal change induced by the driving field. We then derive nonlinear pseudospin oscillator equations for the x and y pseudospin component deviations $\Delta\tilde{\rho}^{(\nu)}_{1,2}(\mathbf{k})$ by taking the second time derivatives of Eqs. (6). Substituting the decomposition (20) in the resulting coupled nonlinear equations, we obtain driven coupled oscillator equations of motion that describe the nonthermal deviations $\Delta\tilde{\rho}^{(\nu)}_{1,2}(\mathbf{k})$ of the transverse pseudospin components along the x and y axes:

$$
\begin{aligned}
&\partial_t^2\,\Delta\tilde{\rho}^{(\nu)}_1(\mathbf{k}) + \left[E_\nu^2(\mathbf{k}) + 4|\Delta_\nu|^2\sin^2\Delta\theta_\nu\right]\Delta\tilde{\rho}^{(\nu)}_1(\mathbf{k}) \\
&\quad + [\partial_t E_\nu(\mathbf{k}) + 2|\Delta_\nu|^2\sin 2\Delta\theta_\nu]\,\Delta\tilde{\rho}^{(\nu)}_2(\mathbf{k}) \\
&= S^{(1)}_\nu(\mathbf{k}) - [\partial_t\delta\Delta''_\nu - \delta\Delta'_\nu E_\nu(\mathbf{k})]N_\nu(\mathbf{k}),\; \partial_t^2\,\Delta\tilde{\rho}^{(\nu)}_2(\mathbf{k}) \\
&\quad + \left[E_\nu^2(\mathbf{k}) + 4|\Delta_\nu|^2\cos^2\Delta\theta_\nu\right]\Delta\tilde{\rho}^{(\nu)}_2(\mathbf{k}) \\
&\quad + [-\partial_t E_\nu(\mathbf{k}) + 2|\Delta_\nu|^2\sin 2\Delta\theta_\nu]\,\Delta\tilde{\rho}^{(\nu)}_1(\mathbf{k}) \\
&= S^{(2)}_\nu(\mathbf{k}) - [\partial_t\delta\Delta'_\nu + \delta\Delta''_\nu E_\nu(\mathbf{k})]N_\nu(\mathbf{k}), \qquad (21)
\end{aligned}
$$

where $\Delta\theta_\nu(t) = \delta\theta_\nu - \delta\theta_\nu^0$ describes the canting of the pseudospins away from their equilibrium directions. The latter directions are determined by $\delta\theta_\nu^0 = 0, \pi$ ($\delta\theta_\nu^0 = 0$) for $s_\pm$ (s_{++}) order-parameter symmetry. In Eq. (21) we defined real and imaginary parts of the SC order parameters Δ'_ν and Δ''_ν, respectively, as

$$
\begin{aligned}
\Delta'_\nu &= |\Delta_\nu|\cos\Delta\theta_\nu = -\sum_{\lambda,\mathbf{k}} g_{\nu,\lambda}\,\tilde{\rho}^{(\lambda)}_1(\mathbf{k}), \\
\Delta''_\nu &= |\Delta_\nu|\sin\Delta\theta_\nu = \sum_{\lambda,\mathbf{k}} g_{\nu,\lambda}\,\tilde{\rho}^{(\lambda)}_2(\mathbf{k}). \qquad (22)
\end{aligned}
$$

Equation (21) describes two coupled driven oscillators. The two terms on the right-hand side of Eqs. (21) are the driving forces, which drive the oscillators at frequencies $\sim 2\omega_0$ as well as at the SC elementary excitation frequencies. The first terms on the right-hand side, $S^{(1,2)}_\nu(\mathbf{k})$, come from sum- and difference-frequency Raman as well as from quantum

transport processes [10]:

$$
\begin{aligned}
S^{(1)}_\nu(\mathbf{k}) =\ & -\left[\Delta E_\nu^2(\mathbf{k}) + 4|\Delta_\nu|^2\sin^2\Delta\theta_\nu\right]\tilde{\rho}^{(\nu),0}_1(\mathbf{k}) \\
& + \Delta[N_\nu(\mathbf{k})E_\nu(\mathbf{k})]\big|\Delta^0_\nu\big| \\
& - |\Delta_\nu|\sin\Delta\theta_\nu\big[e\,\mathbf{E}\cdot\nabla_{\mathbf{k}_+}\big[\tilde{\rho}^{(\nu)}_0(\mathbf{k}_+) + \tilde{\rho}^{(\nu)}_3(\mathbf{k}_+)\big] \\
& + e\,\mathbf{E}\cdot\nabla_{\mathbf{k}_-}\big[\tilde{\rho}^{(\nu)}_0(\mathbf{k}_-) - \tilde{\rho}^{(\nu)}_3(\mathbf{k}_-)\big]\big], \\[4pt]
S^{(2)}_\nu(\mathbf{k}) =\ & [\partial_t E_\nu(\mathbf{k}) - 2|\Delta_\nu|^2\sin 2\Delta\theta_\nu]\,\tilde{\rho}^{(\nu),0}_1(\mathbf{k}) \\
& - |\Delta_\nu|\cos\Delta\theta_\nu\big[e\,\mathbf{E}\cdot\nabla_{\mathbf{k}_+}\big[\tilde{\rho}^{(\nu)}_0(\mathbf{k}_+) + \tilde{\rho}^{(\nu)}_3(\mathbf{k}_+)\big] \\
& + e\,\mathbf{E}\cdot\nabla_{\mathbf{k}_-}\big[\tilde{\rho}^{(\nu)}_0(\mathbf{k}_-) - \tilde{\rho}^{(\nu)}_3(\mathbf{k}_-)\big]\big]. \qquad (23)
\end{aligned}
$$

The second terms on the right-hand side of Eq. (21), proportional to the light-induced deviations $\delta\Delta^{(\nu)}_1$ and $\delta\Delta^{(\nu)}_2$ of the order parameters from their equilibrium values, describe the collective effects, including the Higgs and Leggett collective modes generated by the coupling of all $\mathbf{k}$-point pseudospins. The excitation energies are given by the left-hand side of Eq. (21), which determines the frequencies of the coupled x and y pseudospin oscillators. These frequencies describe pseudospin precession around the time-dependent magnetic field

$$
\mathbf{B}_{\mathbf{k},\nu}(t) = \begin{bmatrix} -2|\Delta_\nu|\cos\Delta\theta_\nu \\ 2|\Delta_\nu|\sin\Delta\theta_\nu \\ E_\nu(\mathbf{k}) \end{bmatrix}. \qquad (24)
$$

The transverse x and y components of this magnetic field are given by the real and imaginary parts of the order parameters, Eq. (22). In particular, the y component is generated by light-induced relative phase oscillations $\Delta\theta_\nu(t) \neq 0$. On the other hand, the time dependence of the longitudinal magnetic field z component is determined by the condensate momentum, with additional contributions from the time-dependent effective chemical potential. The latter, however, does not play an important role for our results here. The oscillator frequencies are determined by $\sqrt{[B^z_{\mathbf{k},\nu}(t)]^2 + [B^y_{\mathbf{k},\nu}(t)]^2}$ ($\Delta\tilde{\rho}^{(\nu)}_1$) and by $\sqrt{[B^z_{\mathbf{k},\nu}(t)]^2 + [B^x_{\mathbf{k},\nu}(t)]^2}$ ($\Delta\tilde{\rho}^{(\nu)}_2$). Importantly, they depend on the time-dependent coupling between the two transverse components, given by $\pm\partial_t B^z_{\mathbf{k},\nu}(t) + B^x_{\mathbf{k},\nu}(t)B^y_{\mathbf{k},\nu}(t)$. The latter transverse light-induced coupling does not contribute to the third-order response. It becomes important in multiband SCs when enhanced by the dynamics of the phase difference between electron and hole pockets, $\Delta\theta_\nu(t)$. As we show below, in the case of strong interband coupling exceeding the intraband interaction, the product $B^x_{\mathbf{k},\nu}(t)B^y_{\mathbf{k},\nu}(t)$ is enhanced by a light-induced relative-phase collective mode of the nonequilibrium SC state. Unlike for the strongly damped Leggett mode, this phase mode at the Higgs frequency is underdamped. The resulting long-lived superconductivity state is characterized by second-harmonic (Floquet) sidebands at bi-Higgs frequencies in the THz-MDCS spectra, discussed in Sec. V B.

To elaborate further, the above nonequilibrium state is driven by the time-dependent coupling term

$$
\begin{aligned}
&[\partial_t E_\nu(\mathbf{k}) - 2|\Delta_\nu|^2\sin 2\Delta\theta_\nu(t)]\Delta\rho^{(\nu)}_1 \\
&= \{e\,[\mathbf{E}(t)\cdot\nabla_{\mathbf{k}}](\mathbf{p}_S\cdot\nabla_{\mathbf{k}})\,\xi_\nu(\mathbf{k}) \\
&\quad - 2|\Delta_\nu|^2\sin 2\Delta\theta_\nu(t)\}\Delta\rho^{(\nu)}_1 + O(\mathbf{p}_S^2), \qquad (25)
\end{aligned}
$$

where we expanded the band dispersions in powers of the center-of-mass momentum $\mathbf{p}_S(t)$ in the last step. The time dependence of the first term of Eq. (25) drives pseudospins via difference-frequency Raman processes $\omega_{A,B} - \omega_{A,B} \sim 0$ and sum-frequency Raman processes $\omega_{A,B} + \omega_{A,B} \sim 2\omega_0$. Here, ω_0 is the center frequency of the applied two laser pulses, which are denoted by A and B. This term contributes beyond the previously studied third-order nonlinear response and leads to the formation of sidebands at Leggett and Higgs mode energies in the THz-MDCS spectra, discussed in Secs. IV A and IV B. The second term of Eq. (25) describes parametric driving of pseudospins by the amplitude and phase collective mode oscillations of the driven system. As we show in Sec. V B, second-harmonic sidebands at bi-Higgs frequency $\sim 2\omega_{H,h}$ thus emerge in the THz-MDCS spectra above critical driving, but only for multiband SC systems with strong interband coupling exceeding intraband interaction. In general, the two different processes described by Eq. (25) are competing. The result of this competition depends on the electric field strength of the applied laser pulses, as well as on the DC current induced by electromagnetic pulse propagation. In Sec. V B we discuss the experimental signatures of the two different processes.

To illustrate further the light induced $\Delta\tilde{\rho}^{(\nu)}(\mathbf{k})$ driven by $\Delta\theta_\nu(t)$, we may transform the equations of motion (6) to the rotated frame defined by the angle $\Delta\theta_\nu(t)$:

$$P_1^{(\nu)}(\mathbf{k}) = \tilde{\rho}_1^{(\nu)}(\mathbf{k})\cos\Delta\theta_\nu - \tilde{\rho}_2^{(\nu)}(\mathbf{k})\sin\Delta\theta_\nu,$$
$$P_2^{(\nu)}(\mathbf{k}) = \tilde{\rho}_1^{(\nu)}(\mathbf{k})\sin\Delta\theta_\nu + \tilde{\rho}_2^{(\nu)}(\mathbf{k})\cos\Delta\theta_\nu'. \quad (26)$$

In this rotating frame, the SC Bloch equations take the form

$$\frac{\partial}{\partial t}\tilde{\rho}_0^{(\nu)}(\mathbf{k}) = -e\,\mathbf{E}(t)\cdot\nabla_{\mathbf{k}}\tilde{\rho}_3^{(\nu)}(\mathbf{k})$$
$$\qquad\qquad - |\Delta_\nu|[P_2^{(\nu)}(\mathbf{k}_-) - P_2^{(\nu)}(\mathbf{k}_+)],$$
$$\frac{\partial}{\partial t}P_1^{(\nu)}(\mathbf{k}) = -[E_\nu(\mathbf{k}) + \partial_t\Delta\theta_\nu]P_2^{(\nu)}(\mathbf{k}),$$
$$\frac{\partial}{\partial t}P_2^{(\nu)}(\mathbf{k}) = [E_\nu(\mathbf{k}) + \partial_t\Delta\theta_\nu]P_1^{(\nu)}(\mathbf{k}) - |\Delta_\nu|N_\nu(\mathbf{k}),$$
$$\frac{\partial}{\partial t}\tilde{\rho}_3^{(\nu)}(\mathbf{k}) = -e\,\mathbf{E}(t)\cdot\nabla_{\mathbf{k}}\tilde{\rho}_0^{(\nu)}(\mathbf{k})$$
$$\qquad\qquad - |\Delta_\nu|[P_2^{(\nu)}(\mathbf{k}_-) + P_2^{(\nu)}(\mathbf{k}_+)]. \quad (27)$$

Analogously to the discussion above, we take the second derivative of Eq. (27) and obtain

$$\partial_t^2\,\Delta P_2^{(\nu)}(\mathbf{k}) + [[E_\nu(\mathbf{k}) + \partial_t\Delta\theta_\nu]^2 + 4|\Delta_\nu|^2]\Delta P_2^{(\nu)}(\mathbf{k})$$
$$- [\partial_t E_\nu(\mathbf{k}) + \partial_t^2\Delta\theta_\nu]\,\Delta P_1^{(\nu)}(\mathbf{k}) = S_\nu(\mathbf{k}) + \partial_t|\Delta_\nu|N_\nu(\mathbf{k}),$$
$$\partial_t\Delta P_1^{(\nu)}(\mathbf{k}) = -[E_\nu(\mathbf{k}) + \partial_t\Delta\theta_\nu]\,\Delta P_2^{(\nu)}(\mathbf{k}), \quad (28)$$

with driving source term

$$S_\nu(\mathbf{k}) = [\partial_t E_\nu(\mathbf{k}) + \partial_t^2\Delta\theta_\nu]\,P_1^{(\nu),0}(\mathbf{k})$$
$$- |\Delta_\nu|[e\,\mathbf{E}\cdot\nabla_{\mathbf{k}_+}[\tilde{\rho}_0^{(\nu)}(\mathbf{k}_+) + \tilde{\rho}_3^{(\nu)}(\mathbf{k}_+)]$$
$$+ e\,\mathbf{E}\cdot\nabla_{\mathbf{k}_-}[\tilde{\rho}_0^{(\nu)}(\mathbf{k}_-) - \tilde{\rho}_3^{(\nu)}(\mathbf{k}_-)]]. \quad (29)$$

The nonlinear oscillator equations (28) are formally equivalent to the parametric oscillator equations of a one-band

superconductor derived in Ref. [10]. In multiband superconductors with strong interband coupling, the pseudospin deviations from equilibrium, determined by the time-dependent rotating frame angle $\Delta\theta(t)$, generate high-order sidebands in the THz-MDCS spectra at high driving fields. These sidebands are analogous to Floquet sidebands, as demonstrated in Sec. IV B.

According to Eqs. (14) and (19), the THz-MDCS nonlinear signal E_{NL} follows from the dynamics of $\tilde{\rho}_0^{(\nu),NL}(\mathbf{k}) = \tilde{\rho}_0^{(\nu),AB}(\mathbf{k}) - \tilde{\rho}_0^{(\nu),A}(\mathbf{k}) - \tilde{\rho}_0^{(\nu),B}(\mathbf{k})$. Here, $\tilde{\rho}_0^{(\nu),AB}(\mathbf{k})$ denotes the gauge-invariant density matrix of the nonequilibrium state driven by both pulses. $\tilde{\rho}^{(\nu),A}(\mathbf{k})$ [$\tilde{\rho}^{(\nu),B}(\mathbf{k})$] is the gauge-invariant density matrix of the nonequilibrium state driven by pulse A (B). For interpreting the results of the full numerical calculation, it is useful to distinguish between nonlinear processes due to the excitations by a single pulse that are sensed by the other pulse and the excitations generated by *both* pulses simultaneously. These two different processes lead to different experimental features. For this, we decompose the density matrix $\tilde{\rho}^{(\nu),AB}(\mathbf{k})$ as

$$\tilde{\rho}^{(\nu),AB}(\mathbf{k}) = \tilde{\rho}^{(\nu),A}(\mathbf{k}) + \tilde{\rho}^{(\nu),B}(\mathbf{k}) + \Delta\tilde{\rho}^{(\nu),AB}(\mathbf{k}), \quad (30)$$

where $\Delta\tilde{\rho}^{(\nu),AB}(\mathbf{k})$ is generated by interference between SC excitations of both pulses A and B. Inserting Eq. (30) into the equation of motion for $\tilde{\rho}_0^{(\nu),NL}(\mathbf{k})$ leads to

$$\frac{\partial}{\partial t}\tilde{\rho}_0^{(\nu),NL}(\mathbf{k}) = -e\,\mathbf{E}_B(t)\cdot\nabla_{\mathbf{k}}\tilde{\rho}_3^{(\nu),A}(\mathbf{k})$$
$$- |\Delta_\nu^A|\nabla_{\mathbf{k}}(\tilde{\rho}_2^{(\nu),A}(\mathbf{k}) + \Delta\theta_A\tilde{\rho}_1^{(\nu),A}(\mathbf{k}))\,\mathbf{p}_S^B$$
$$- |\Delta_\nu^A|\nabla_{\mathbf{k}}(\tilde{\rho}_2^{(\nu),B}(\mathbf{k}) + \Delta\theta_A\tilde{\rho}_1^{(\nu),B}(\mathbf{k}))\,\mathbf{p}_S^B$$
$$- |\Delta_\nu^A|\nabla_{\mathbf{k}}(\tilde{\rho}_2^{(\nu),B}(\mathbf{k}) + \Delta\theta_A\tilde{\rho}_1^{(\nu),B}(\mathbf{k}))\,\mathbf{p}_S^A$$
$$- |\Delta_\nu^A|\Delta\theta_B\nabla_{\mathbf{k}}(\tilde{\rho}_1^{(\nu),A}(\mathbf{k})\,\mathbf{p}_S^B + \tilde{\rho}_1^{(\nu),B}(\mathbf{k})\,\mathbf{p}_S^A$$
$$+ \tilde{\rho}_1^{(\nu),A}(\mathbf{k})\,\mathbf{p}_S^A + \tilde{\rho}_1^{(\nu),B}(\mathbf{k})\,\mathbf{p}_S^B)$$
$$+ \Delta\tilde{\rho}^{(\nu),AB} + O(\mathbf{p}_S^2) + O[(\Delta\theta)^2] + A \leftrightarrow B, \quad (31)$$

where we expanded in terms of $\mathbf{p}_S$ and $\Delta\theta$ and neglected all contributions of order $O(\mathbf{p}_S^2)$ and $O[(\Delta\theta)^2]$. The terms in the first two lines of Eq. (31) contribute to the nonlinear response when pulse B arrives after pulse A to sense the SC excitations by pulse A, as in conventional pump-probe spectroscopy. This signal exists even if the two pulses do not overlap in time. The corresponding contribution to the THz-MDCS spectra shows up in our results as harmonic sidebands ($\pm\omega_0$) around the quasiparticle, Higgs and Legget mode frequencies. The THz-MDCS spectral peaks at high driving fields are mainly generated by the terms in the third line on the right-hand side of Eq. (31), which dominate over the other terms in the nonperturbative excitation regime. Here, the observed signals only appear along $(\omega_t, 0)$, i.e., along the frequency vector of pulse A, $\omega_A = (\omega_0, 0)$, and along $(\omega_t, -\omega_t)$, i.e., along the frequency vector of pulse B, $\omega_B = (\omega_0, -\omega_0)$. The $\Delta\tilde{\rho}^{(\nu),AB}$ contributions result from the interference between SC excitations of pulses A and B and lead to the correlated wave-mixing peaks discussed in Ref. [10]. The latter new signals arise from parametric driving of superconductivity by the pump-probe coherent modulation of the order parameter by *both* pulses A

and B. In this paper, we consider a different pulse excitation scheme from Ref. [10], with two strong few-cycle pulses of similar *broad* spectral shape. For this excitation protocol, the $\Delta\tilde{\rho}^{(v),AB}(\mathbf{k})$ interference terms only contribute to the THz-MDCS spectra at low fields. These $\Delta\tilde{\rho}^{(v),AB}$ contributions are discussed in more detail in Appendix C.

IV. THZ-MDCS WITHOUT PERSISTENT SYMMETRY BREAKING

To demonstrate the importance of the electromagnetic propagation effects in determining the effective driving field, we first consider in this section a driving field given by the laser pulse $E_{THz}(t)$, instead of the effective local pulse (15). The Cooper-pair momentum $\mathbf{p}_S(t)$ then vanishes after the pulse, as in previous theories. First we present the spectra as a function of the driving pulse-pair strength with interband interaction set to zero. Then, we show how these spectra change for finite interband interaction.

A. Zero interband interaction

We start with the calculation of the THz-MDCS spectrum by setting the interband interaction to zero, $g_{e,h} = 0$. The results of this calculation with uncoupled bands extend the corresponding one-band results of Ref. [10], obtained for excitation by a strong narrow-band pump and a weak broadband probe, to the case of excitation by a pair of few-cycle pulses with identical broad spectral shape and strength. The choice of excitation protocol is important for controlling the different nonlinear process that can dominate the THz-MDCS.

We first make a connection with previous works by calculating the order-parameter dynamics driven by a single pump pulse with $g_{e,h} = 0$. The upper panel of Fig. 2 shows the time dependence of (a) the hole-pocket order-parameter amplitude $2|\Delta_h|$, and (b) the electron-pocket order-parameter amplitude $2|\Delta_e|$. It compares between four different electric field strengths in the case of resonant excitation of the hole-pocket SC gap. The corresponding order-parameter spectra are presented in Figs. 2(c) and 2(d). For weak excitation (blue line), both electron and hole order parameters show second-harmonic oscillations, with frequency $2\omega_0 = 2$ THz, which occur during the short pulse [vertical magenta lines in Figs. 2(c) and 2(d)]. These harmonic oscillations are followed by damped Higgs mode oscillations with frequencies $\omega_{H,v} = 2\Delta_{\infty,v}$, where $\Delta_{\infty,v}$ are the quenched order parameters of the steady state after the pulse. For the weakest driving field studied here (blue line), $\omega_{H,h} \sim 2\omega_0$ due to near-resonant excitation across the equilibrium state energy gap. As a result, we only observe a single resonance since the Higgs frequency $\omega_{H,h}$ overlaps with the second-harmonic resonance at $2\omega_0$. With increasing driving field, however, the SC order parameter of the hole pocket is quenched in the nonequilibrium steady state as compared to the initial state. This quantum quench of the order parameter occurs via difference-frequency Raman processes [10] during cycles of field oscillations, which results in a low-frequency coherent enhancement of $2|\Delta_h|$. It also results in a redshift of the Higgs mode frequency $\omega_{H,h} = 2\Delta_{\infty,h} < 2\Delta_{0,h} = 2\omega_0$ [vertical dashed black line in Fig. 2(c)]. As seen in Fig. 2(c), with increasing field, the
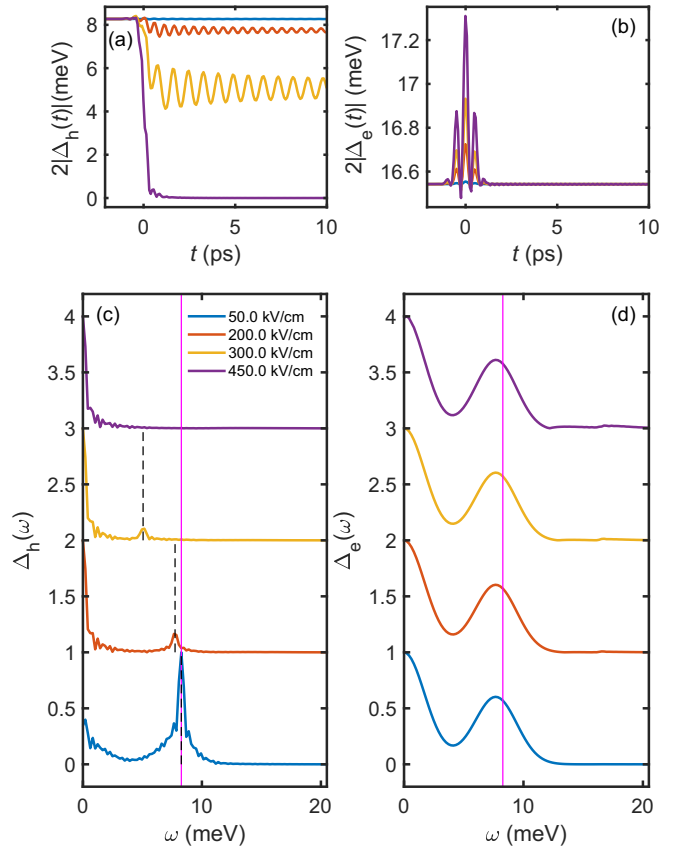

FIG. 2. THz-driven nonequilibrium order-parameter dynamics. Time evolution of (a) the order-parameter amplitude of the hole pocket $2|\Delta_h|$, and (b) the order-parameter amplitude of the electron pocket $2|\Delta_e|$ for four different driving fields. The corresponding spectra are shown in (c) and (d). Traces are offset for clarity. The vertical magenta line indicates the second-harmonic resonance at $\omega = 2\omega_0$, while the Higgs mode frequency of the hole pocket $\omega_{H,h}$ is marked by vertical dashed black lines.

low-frequency enhancement of the order-parameter spectrum dominates over the Higgs mode resonance. The latter peak vanishes completely for the highest studied driving field (purple line). Compared to the hole pocket, the spectrum of $2|\Delta_e|$ in the electron pocket always shows a broad second-harmonic peak (vertical magenta line), which increases with growing field strength. There is no Higgs mode peak there. The difference in the dynamics between hole and electron pockets is due to the off-resonant excitation condition $2\omega_0 \ll \omega_{H,e}$ for the electron band.

To fully characterize the nonequilibrium condensate state, we must turn to the THz-MDCS spectra. Figures 3(a) and 3(b) show two examples of the calculated nonlinear differential field $E_{NL}(t, \tau)$ as a function of real time t and interpulse time delay τ. By comparing the results obtained with electric fields of 50 and 300 kV/cm, we observe a change in the overall time dependence with increasing field. For low driving [Fig. 3(a)], the oscillations along the t and τ axes are determined by the laser frequency ω_0. As seen by comparing with Fig. 3(b), the oscillation frequencies change for the higher field. To identify the nonlinear processes leading to this change, we study the THz-MDCS spectra obtained by Fourier
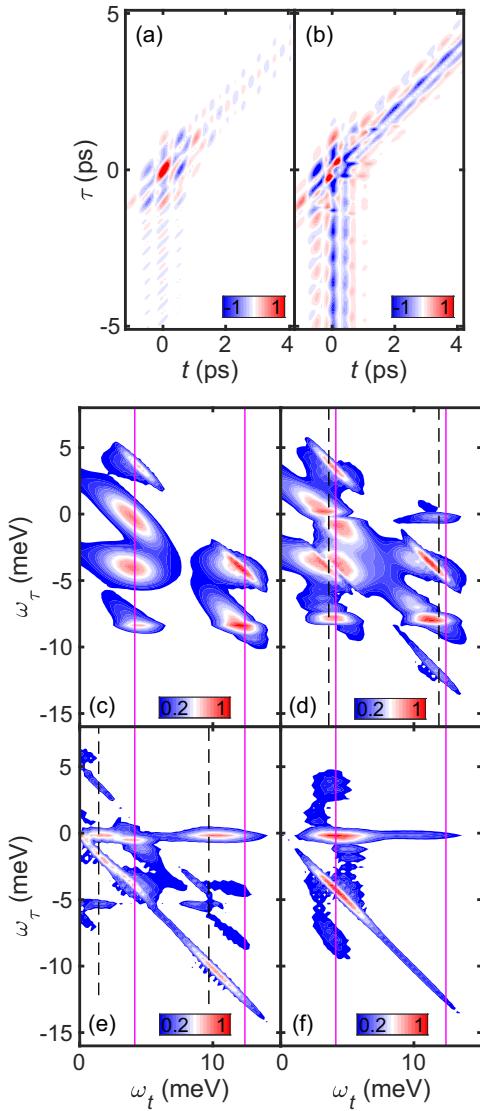
FIG. 3. THz-MDCS of a multiband SC system with negligible interband interaction. Normalized $E_{\mathrm{NL}}(t, \tau)$ as a function of real time t and interpulse delay τ for an electric field strength of (a) 50 kV/cm and (b) 300 kV/cm. (c)–(f) THz-MDCS spectra $E_{\mathrm{NL}}(\omega_t, \omega_\tau)$ for an electric field strength of (c) 50 kV/cm, (d) 200 kV/cm, (e) 300 kV/cm, and (f) 450 kV/cm. Vertical magenta lines indicate $\omega_t = \omega_0$ and $\omega_t = 3\omega_0$ while $\omega_t = \omega_{\mathrm{H,h}} \pm \omega_0$ are marked by vertical dashed black lines.

transform of $E_{\mathrm{NL}}(t, \tau)$ with respect to both t (frequency ω_t) and τ (frequency ω_τ). Figures 3(c)–3(e) show the $E_{\mathrm{NL}}(\omega_t, \omega_\tau)$ two-dimensional spectra for the four driving fields studied in Fig. 2. We compare the positions of the THz-MDCS peaks with respect to the laser pulse frequency vectors $\omega_{\mathrm{A}} = (\omega_0, 0)$ and $\omega_{\mathrm{B}} = (\omega_0, -\omega_0)$, which determine the positions of the peaks in semiconductors and other conventional materials. For the weakest studied field [Fig. 3(c)], the order parameters remain close to their equilibrium values. Similar to semiconductors, the quasiparticle excitation energy gap then does not change from equilibrium. As a result, the THz-MDCS spectrum in Fig. 3(c) shows peaks at multiples of the laser frequency ω_0. This behavior is similar to semiconductors

[2,50] and recovers the results of a perturbative susceptibility analysis [10]. The peaks observed in Fig. 3(c) can be attributed to the third-order nonlinear responses of the equilibrium SC state. These can be described by using the third-order susceptibility, which in superconductors measures the elementary excitations of the equilibrium state that do not contribute to the linear response. Figure 3(c) displays the conventional pump-probe (PP) peaks at $(\omega_t, \omega_\tau) = (\omega_0, 0)$ and $(\omega_0, -\omega_0)$, which are generated by the nonlinear processes $(\omega_{\mathrm{B}} - \omega_{\mathrm{B}}) + \omega_{\mathrm{A}}$ and $(\omega_{\mathrm{A}} - \omega_{\mathrm{A}}) + \omega_{\mathrm{B}}$, respectively. The peaks at $(\omega_0, -2\omega_0)$ and (ω_0, ω_0) correspond to four-wave-mixing signals arising from the processes $(\omega_{\mathrm{B}} - \omega_{\mathrm{A}}) + \omega_{\mathrm{B}}$ and $(\omega_{\mathrm{A}} - \omega_{\mathrm{B}}) + \omega_{\mathrm{A}}$. Finally, third-harmonic generation peaks are visible at $(3\omega_0, -2\omega_0)$ and $(3\omega_0, -\omega_0)$. These conventional third-order nonlinear peaks characterize the dynamics of a SC elementary excitation, quasiparticle, or collective mode. As known from previous works, quasiparticle excitations dominate over the Higgs collective mode contributions in this case.

With increasing driving field, the THz quantum quench of the SC order parameter separates the excitation energy of the nonequilibrium state $\omega_{\mathrm{H,h}} = 2\Delta_{\infty,\mathrm{h}}$ from the second-harmonic frequency $2\omega_0 \sim 2\Delta_{0,\mathrm{h}}$ that excites the equilibrium state energy gap. Figure 3(d) then shows multiple new THz-MDCS peaks. In particular, Fig. 3(d) displays strong peaks at frequencies $\omega_t = \omega_{\mathrm{H,h}} \pm \omega_0$ (dashed black lines), which split from the pump-probe and third-harmonic generation peaks of Fig. 3(c) (solid magenta lines). These new peaks are mainly generated by contributions to the current (14) arising from the source terms of the form $\sim \tilde{\rho}_2^{(v),\mathrm{A}}(\mathbf{k})\, \mathbf{p}_{\mathrm{S}}^{\mathrm{B}}$ in the second term on the right-hand side of Eq. (31). Such nonlinear contributions reflect the time dependence of the excitations of the nonequilibrium SC state, which give oscillations of the pseudospin component $\tilde{\rho}_2^{(v),\mathrm{A,B}}(\mathbf{k})$ at frequencies $\sim \omega_{\mathrm{H,h}}$ that are sensed by the other pulse ($\mathbf{p}_{\mathrm{S}}^{\mathrm{B,A}}$). The contribution of these excitations to the THz-MDCS mainly arises when pulse B (A) arrives after the pulse A (B) driving the $\omega_{\mathrm{H,h}}$ excitation. This nonlinear signal does not require any interference or interaction between excitations by different pulses. For high fields, it measures the dynamics of a single nonequilibrium SC state excitation by one pulse (Fig. 2), which is probed by the other pulse.

The THz-MDCS signal and additional peaks observed in Fig. 3(d) cannot be attributed to the Higgs collective mode. In particular, our calculated $\tilde{\rho}_2^{(v)}(\mathbf{k})$ spectra are dominated by $\mathbf{k}$-dependent peaks centered at the quasiparticle continuum energies $E_{\mathbf{k}}^{\mathrm{qp,(h)}} = 2\sqrt{E_{\mathrm{h}}^2(\mathbf{k}) + |\Delta_{\infty,h}|^2}$. This is the case for the few-cycle broadband pulses used in this paper [10]. The largest contribution of $\tilde{\rho}_2^{(v)}(\mathbf{k})$ stems from the quasiparticle excitations in proximity to the excitation energy minimum (energy gap $\sim \omega_{\mathrm{H,h}}$). The second term on the right-hand side of Eq. (31) then generates the third-order nonlinear processes $\omega_{\mathrm{H,h;A}} \pm \omega_{\mathrm{B}}$, where $\omega_{\mathrm{H,i;A}} = (\omega_{\mathrm{H,i}}, 0)$ ($i = $ e, h) describes a single SC excitation by pulse A. These processes lead to THz-MDCS peaks at $(\omega_{\mathrm{H,h}} - \omega_0, \omega_0)$ and $(\omega_{\mathrm{H,h}} + \omega_0, -\omega_0)$ [dashed black lines in Fig. 3(d)]. These peaks split from the conventional PP and HHG peaks of Fig. 3(c), which are located at (ω_0, ω_0) and $(3\omega_0, -\omega_0)$, as $\omega_{\mathrm{H,h}} < 2\omega_0$ with increasing field. Exchanging labels A and B gives the third-order nonlinear processes $\omega_{\mathrm{H,h;B}} \pm \omega_{\mathrm{A}}$ where $\omega_{\mathrm{H,i;B}} = (\omega_{\mathrm{H,i}}, -\omega_{\mathrm{H,i}})$ ($i = $ e, h), which generate peaks

at $(\omega_{H,h} - \omega_0, -\omega_{H,h})$ and $(\omega_{H,h} + \omega_0, -\omega_{H,h})$. We conclude that the above THz-MDCS peaks mostly characterize the dynamics of the quasiparticle excitations of the SC steady state with quenched energy gap.

The THz-MDCS spectrum shows four additional competing peaks, two along direction $(\omega_t, 0)$ and two along $(\omega_t, -\omega_t)$. By increasing the driving field further, Fig. 3(e) shows that the latter signals, with peaks at two-dimensional (2D) frequencies $\sim(\omega_{H,h} \pm \omega_0, -\omega_{H,h} \mp \omega_0)$ and $\sim(\omega_{H,h} \pm \omega_0, 0)$, dominate over the third-order signals at $\omega_t = \omega_{H,h} \pm \omega_0$ in Fig. 3(d). We next discuss their origin. For the field strength of 300 kV/cm used in Fig. 3(e), the SC order parameter of the hole pocket is strongly quenched by the difference-frequency coherent Raman process $2\omega_A - 2\omega_A$. As seen in Fig. 2(c) (yellow curve, black dashed line), the resulting peak of the $|\Delta_h^A|$ spectrum at $\omega \sim 0$ dominates over the peak at $\omega_{H,h}$ (black dashed line). At the same time, $\Delta\tilde{\rho}_2^{(\nu)}$ in Eq. (21) is driven by the source term (25). Without interband interaction, the latter time-dependent transverse canting is driven by the condensate acceleration leading to $\partial_t E_\nu(\mathbf{k}) \neq 0$. Equation (21) describing the coupling between the light-induced x and y pseudospin component deviations from equilibrium then reduces to $\partial_t E_\nu(\mathbf{k})\Delta\rho_1^{(\nu)} \approx e\,(\mathbf{E}(t) \cdot \nabla_\mathbf{k})(\mathbf{p_S} \cdot \nabla_\mathbf{k})\,\xi_\nu(\mathbf{k})\Delta\rho_1^{(\nu)}$. Noting that the $\Delta\tilde{\rho}_1^{(\nu)}(\mathbf{k})$ dynamics is determined by the frequency $\omega_{H,h}$, the source term (25) resonantly drives $\Delta\tilde{\rho}_2^{(\nu)}(\mathbf{k})$ with frequency $\omega_{H,h;B} + (\omega_B - \omega_B)$. Together with the order-parameter quantum quench through the frequency-difference coherent process $2\omega_A - 2\omega_A$, we obtain a signal, determined by the third term on the right-hand side of Eq. (31), that is generated by the high-order nonlinear process $(2\omega_A - 2\omega_A) + \omega_{H,h;B} + (\omega_B - \omega_B) \pm \omega_B$. This higher Raman process is of ninth order with respect to the equilibrium state. It generates THz-MDCS peaks at 2D frequencies $(\omega_{H,h} \pm \omega_0, -\omega_{H,h} \mp \omega_0)$ through a combination of transverse pseudospin canting and order-parameter coherent modulation. In the same way, by exchanging A $\leftrightarrow$ B, we obtain peaks at $(\omega_{H,h} \pm \omega_0, 0)$. Figure 3(e) demonstrates that the above high-order Raman processes dominate over the conventional third-order processes in the THz-MDCS nonlinear spectra for sufficiently strong pulse-pair driving of a nonequilibrium SC steady state. Eventually, in the extreme nonlinear excitation regime [Fig. 3(f)] where the SC order-parameter amplitude $|\Delta_h|$ and corresponding excitation energy gap is completely quenched [purple line in Fig. 2(c)], the THz-MDCS spectral line shape displays sharp pump-probe peaks at $(\omega_0, 0)$ and $(\omega_0, -\omega_0)$ that dominate over the third-harmonic peaks of Fig. 3(c).

We end this section by noting that a comparison of the $U = 0$ few-cycle pulse-pair excitation results with the narrowband strong pump-broadband weak probe results of Ref. [10] suggests that the excitation protocol can be designed to highlight different nonlinear processes in the THz-MDCS spectra (see also Appendix C). In all cases, the main qualitative differences in the spectral profile of superconductors as compared to other systems originate from the coherent modulation of the elementary excitation energy. In particular, THz-MDCS of superconductors measures excitations of the light-induced nonthermal steady state, which differs from the
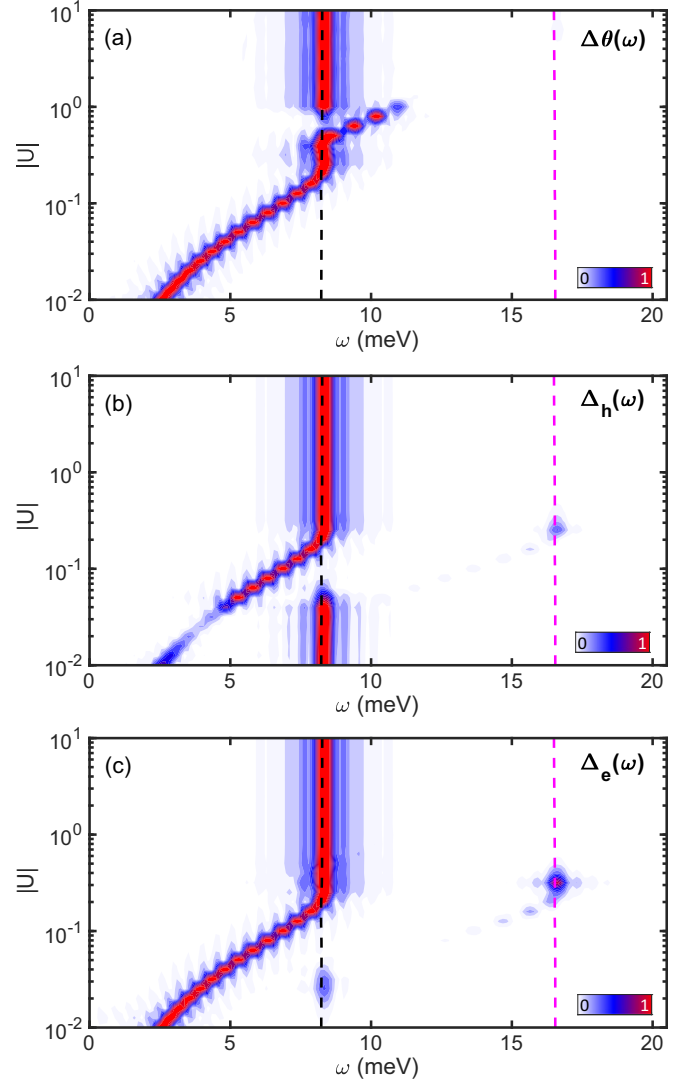

FIG. 4. Dependence of amplitude and relative phase collective modes on the interband interaction strength. (a) $\Delta\theta$ spectrum, (b) $|\Delta_h|$ spectrum, and (c) $|\Delta_e|$ spectrum as a function of interband interaction strength $|U|$ for weak $E_0 = 100.0$ kV/cm excitation. Spectra are normalized to one for a given $|U|$. Dashed black (magenta) line indicates $\omega_{H,h}$ ($\omega_{H,e}$).

equilibrium states. Additional differences arise from nonlinear pseudospin processes driven by the condensate acceleration by the applied THz field, which determine the properties of the time-dependent SC state.

B. Nonzero interband interaction

We now consider how interband interactions can change the above $U = 0$ picture. Before presenting the THz-MDCS results, we first study the multiband order-parameter amplitude and relative phase spectra as a function of the interband interaction. We consider excitation by a single, relatively weak, few-cycle THz electric field, so that we can map the excitations of the equilibrium state for different U. Figure 4 shows the dependence on $|U| = |g_{\lambda,\nu}|/V_h$, $\nu \neq \lambda$, of
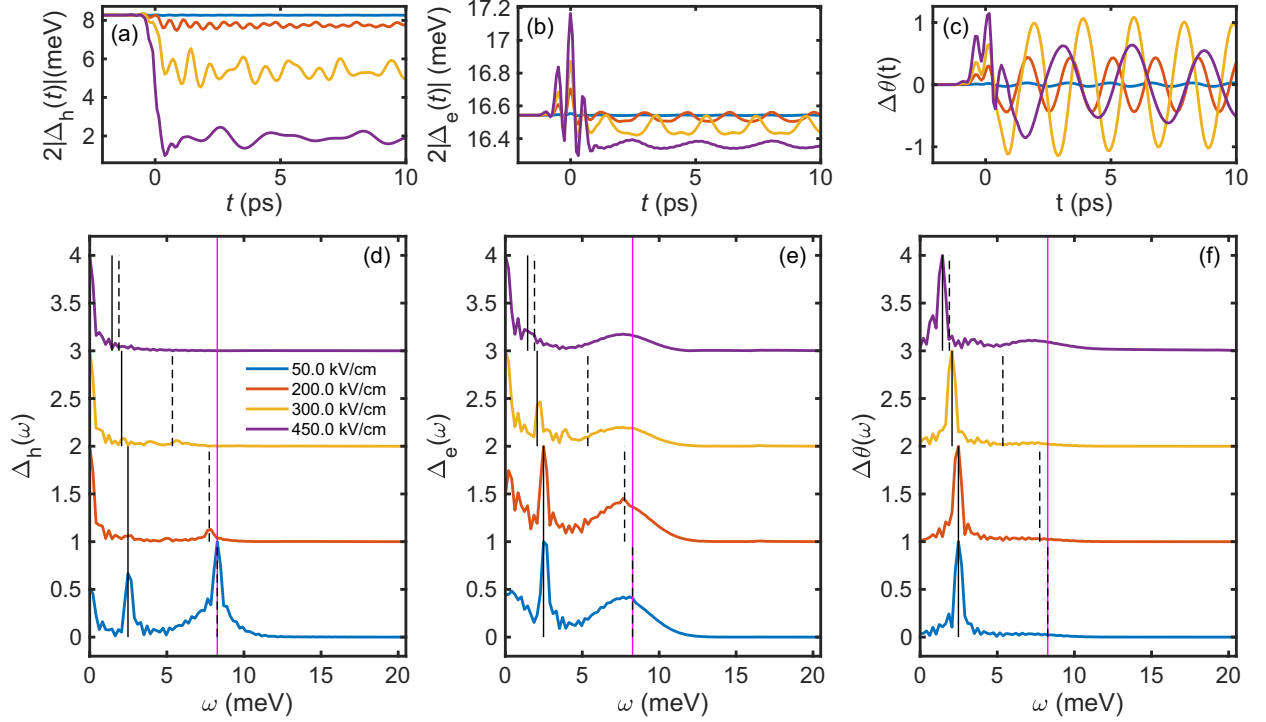
FIG. 5. THz-driven dynamics of amplitude and relative phase modes for weak interband interaction $U = 0.01$ and four different driving fields. Time evolution of (a) the order-parameter amplitude of the hole pocket $2|\Delta_h|$, (b) the order-parameter amplitude of the electron pocket $2|\Delta_e|$, and (c) the relative phase $\Delta\theta$. The corresponding spectra are shown in (d)–(f). Vertical magenta lines indicate the second-harmonic resonance at $\omega = 2\omega_0$ while the Higgs mode frequency of the hole pocket $\omega_{H,h}$ (Leggett mode ω_L) is marked by vertical dashed (solid) black lines.

(a) relative phase spectrum $\Delta\theta(\omega)$, (b) hole order-parameter amplitude spectrum $|\Delta_h|$, and (c) electron order-parameter amplitude spectrum $|\Delta_e|$. In the simulations, we fixed the ratio $U = g_{e,h}/V_h$ and adjusted V_e and V_h to keep $\omega_{H,h}$ and $\omega_{H,e}$ unchanged. A resonance in $\Delta\theta(\omega)$ is seen in Fig. 4(a), which results from a phase collective mode. For small $|U|$, we obtain such a Leggett mode with energy $\omega_L \sim 2.5$ meV. This phase mode lies well below the lower hole-band excitation energy gap $\omega_{H,h}$, which is marked in Fig. 4 by the dashed black line. The position of the Leggett mode within this energy gap agrees with earlier studies on multiband superconductors with dominating intraband interaction [25]. As $|U|$ increases, however, the phase mode blueshifts towards $\omega_{H,h}$ and crosses $\omega_{H,h}$ around $|U| \sim 0.5$. It moves towards $\omega_{H,e}$ (magenta dashed line) as $|U|$ further increases. In this regime of strong $|U|$, the Leggett mode becomes strongly damped, as it is located within the hole-band quasiparticle continuum. As a result, for weak photoexcitation, the effects of the relative phase dynamics on the THz-MDCS are small for large U, unlike for small U. Next, we study how this order-parameter dynamics changes by increasing the driving field, and compare the field dependence between weak and strong interband interactions.

1. Dominant intraband interaction

We first study the behavior of the order parameter for small but finite U, $0 < |U| \ll 1$. This is the case, e.g., in MgB$_2$ superconductors [16,21,25,32,51–54]. The main difference introduced by the small $|U|$ is the emergence of

a Leggett phase mode whose frequency lies within the energy gap. Figure 5 presents the time dependence of (a) the order-parameter amplitude in the hole pocket $2|\Delta_h|$, (b) the order-parameter amplitude in the electron pocket $2|\Delta_e|$, and (c) the phase difference between the electron- and hole-pocket order parameters $\Delta\theta$. These results were obtained for four different electric field strengths with $U = 0.01$. Figure 4 shows that, for such parameters, the Leggett mode is not damped. The corresponding order-parameter spectra are plotted in Figs. 5(d)–5(f). The main difference from the uncoupled band case (Fig. 2) is the emergence of an additional peak in $\Delta\theta(\omega)$ [Fig. 5(f)]. This resonance also appears in the order-parameter amplitude spectra [solid black line in Figs. 5(d) and 5(e)].

In the weak excitation regime (blue line), the $\Delta\theta$ spectrum shows a sharp peak at the Leggett mode energy $\omega_L \sim 2.5$ meV (solid black line). As discussed above, this peak is located well below the low-energy excitation energy gap $\omega_{H,h} \sim 8.2$ meV (dashed black line). This Leggett mode (solid black line) also shows up in the $|\Delta_h|$ ($|\Delta_e|$) amplitude spectrum, in addition to the Higgs mode (dashed black line, $\omega_{H,h}$) and second-harmonic generation ($2\omega_0$, solid magenta line) peaks. This coexistence of phase and amplitude mode peaks demonstrates that the amplitude mode and the phase mode are coupled despite their different frequencies. With increasing field, the Leggett mode slightly redshifts, while the order parameter becomes quenched. The latter coherent quench of the hole and electron order-parameter amplitudes is seen as a low-frequency ($\omega = 0$) enhancement of $|\Delta_h|$ and $|\Delta_e|$ spectra in Figs. 5(d) and 5(e). The order-parameter amplitude quench
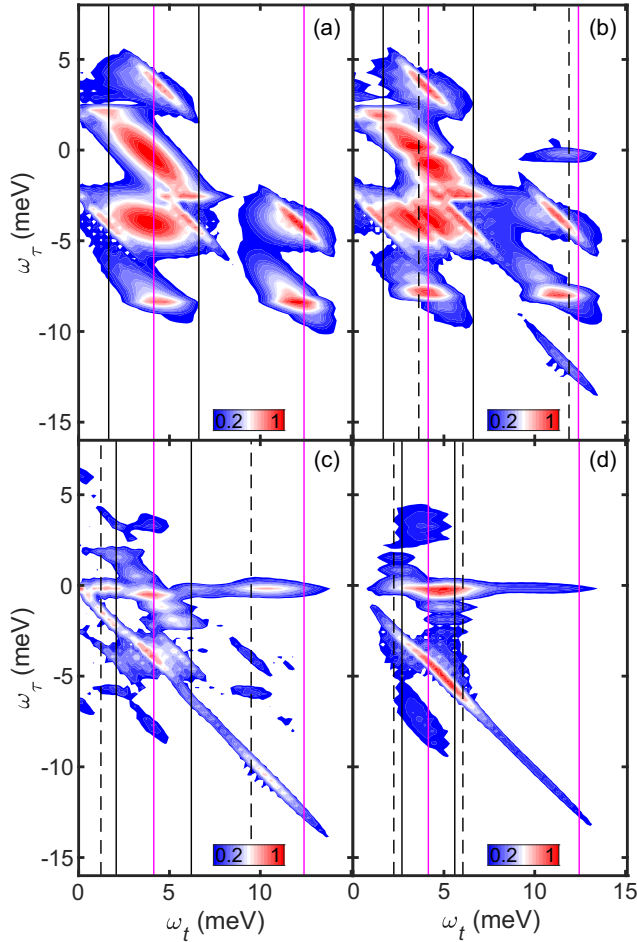
FIG. 6. THz-MDCS of a multiband superconductor with dominant intraband interaction ($\mathbf{p}_S = 0$ after the pulse). Normalized THz-MDCS spectra $E_{NL}(\omega_t, \omega_\tau)$ for an electric field strength of (a) 50 kV/cm, (b) 200 kV/cm, (c) 300 kV/cm, and (d) 450 kV/cm. Vertical magenta lines indicate $\omega_t = \omega_0$ and $\omega_t = 3\omega_0$, while $\omega_t = \omega_{H,h} \pm \omega_0$ ($\omega_t = \omega_0 \pm \omega_L$) are marked by vertical black dashed (solid) lines.

dominates over the collective mode resonances in these amplitude spectra with increasing field, analogously to the case without interband interaction in Fig. 2.

Figure 6 presents the THz-MDCS spectra for the four electric field strengths studied in Fig. 5 with finite U. For low driving field, Fig. 6(a), the THz-MDCS spectrum is dominated by the pump-probe, four-wave-mixing, and third-harmonic peaks discussed in Sec. IV A. The order parameter for this low field (blue curves in Fig. 5) displays sharp Higgs and Leggett modes. By comparing with the corresponding spectra for $U = 0$ [Fig. 3(c)], the presence of the Leggett phase mode for $U \neq 0$ leads to the formation of THz-MDCS satellites (vertical solid black lines) around the $(\omega_0, 0)$ and $(\omega_0, -\omega_0)$ pump-probe peaks. These Leggett mode peaks originate from the fifth term on the right-hand side of Eq. (31), $\propto \Delta\theta(t)\mathbf{p}_s(t)$. In particular, the relative phase oscillations at frequency ω_L (Leggett collective mode) lead to $(\omega_0 \pm \omega_L, -\omega_0)$ peaks [black solid lines in Fig. 6(a)] via the third-order nonlinear processes $\omega_B \pm \omega_{L;A}$, where $\omega_{L;A} = (\omega_L, 0)$. Exchanging

pulses A and B produces similar Leggett mode peaks at $(\omega_0 \pm \omega_L, \mp\omega_L)$, generated by the third-order nonlinear processes $\omega_A \pm \omega_{L;B}$, where $\omega_{L;B} = (\omega_L, -\omega_L)$.

With increasing field [Fig. 5(a) (red line)], the order-parameter coherent quench $\omega_{H,h} < 2\omega_0$ results in the formation of THz-MDCS peaks at $\omega_t = \omega_{H,h} \pm \omega_0$, similar to Sec. IV A. These peaks, marked by the vertical dashed lines in Fig. 6(b), are additional to the relative phase-mode peaks (solid black lines) and the conventional third-order response peaks (solid magenta lines). As the field increases further, Fig. 6(c) shows that, similar to the $U = 0$ case, the THz-MDCS spectrum is dominated by sharp peaks along $(\omega_t, 0)$ and $(\omega_t, -\omega_t)$ directions. The difference from $U = 0$ are peaks at $\omega_t = \omega_0 \pm \omega_L$ marked by vertical solid black lines. These peaks are generated by the nonlinear coupling of the x and y transverse pseudospin components described by Eq. (25). The pseudospins are then driven via sum-frequency nonlinear processes $\omega_0 + \omega_0 + \omega_L$, instead of $\omega_0 - \omega_0 + \omega_{H,h}$ processes. We thus obtain peaks at $\omega_t = \omega_0 \pm \omega_L$ via the ninth-order nonlinear processes $(2\omega_A - 2\omega_A) \pm \omega_{L,B} + (\omega_B + \omega_B) - \omega_B$. These peaks at two-dimensional frequencies $(\pm\omega_L + \omega_0, \mp\omega_L - \omega_0)$ are marked by the solid black lines. Exchanging pulses A and B produces similar peaks at $(\pm\omega_L + \omega_0, 0)$. Finally, for the highest studied field strength of 450 kV/cm, the Leggett mode is close to $\omega_{H,h}$ in Fig. 5 (purple line). As a result, the collective mode and quasiparticle peaks cannot be resolved anymore in the THz-MDCS spectrum of Fig. 6(d). We then obtain broad THz-MDCS peaks around $\omega_t = \omega_0$ (magenta solid line).

2. Dominant interband interaction

We now compare the above THz-MDCS spectral profiles for small U with the case where the interband interaction exceeds the intraband interaction $|U| > 1$. This strong interband coupling condition is realized in several iron-based superconductors [43,49,55,56]. Here we present results for $U = 2$ as in such systems. We first characterize the SC order-parameter dynamics induced by a single pulse. Figure 7 shows the field dependence of (a) the order-parameter amplitude spectrum $|\Delta_h(\omega)|$ and (b) the relative phase spectrum $\Delta\theta(\omega)$. In the weak photoexcitation regime, $|\Delta_h(\omega)|$ exhibits a peak at the Higgs-mode frequency $\omega_{H,h}$ (solid black line). In addition to this Higgs-mode peak, the spectrum of the relative phase $\Delta\theta(\omega)$ in Fig. 7(b) shows a Leggett mode peak. The difference for large U is that the Leggett mode lies within the quasiparticle continuum, $\omega_L \sim 11$ meV $> \omega_{H,h}$, and is thus strongly damped for low fields. With increasing driving field, the $\omega_{H,h}$ mode redshifts slightly. In addition, a new peak emerges in the hole order-parameter spectrum $\Delta_h(\omega)$, at the electron-pocket frequency $\omega_{H,e}$ (dashed black line). This peak is absent for small U and arises from the coherent coupling of the Higgs modes in the electron and hole pockets (hybrid Higgs mode [18]). Light-induced nonlinear couplings of collective modes in different bands coupled via Coulomb interaction have been proposed before to affect the pump-probe spectra via the formation of hybrid modes [57]. Here, a *hybrid Higgs* amplitude collective mode forms due to the strong coupling between the electron and hole pockets for large U [18]. At the same time, the Leggett mode peak redshifts towards
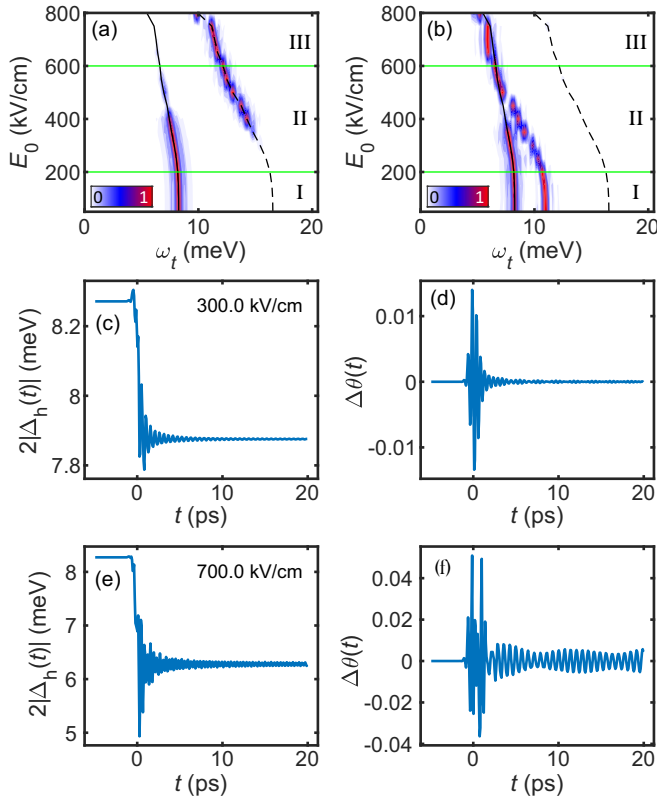
FIG. 7. Dependence of amplitude and relative phase collective modes on the driving-field strength for interband interaction dominating over intraband interaction. Electric field strength dependence of (a) the SC order-parameter spectrum $|\Delta_h|$ and (b) the relative phase spectrum $\Delta\theta$. Spectra are normalized to one for a given E_0. The Higgs mode $\omega_{H,h}$ ($\omega_{H,e}$) is marked with a solid (dashed) black line. Horizontal lines indicate the excitation regimes I–III. (c), (e) $|\Delta_h|$ dynamics for driving fields of 300 kV/cm (c) and 700 kV/cm (e). The corresponding relative phase dynamics is plotted in (d) and (f).

$\omega_{H,h}$. As a result, a new relative phase collective mode forms with frequency around $\omega_{H,h}$. This new mode characterizes the light-driven nonequilibrium SC state and is not observed close to equilibrium. We show below that the relative phase mode parametrically drives the coupled nonlinear harmonic oscillator equations of motion (21) at the frequency $\omega_{H,h}$, via Eq. (25), which results in the formation of dominant bi-Higgs-frequency sidebands in the THz-MDCS spectra, discussed below.

Next, we compare the THz-MDCS spectra in the three excitation regimes indicated by the horizontal lines in Figs. 7(a) and 7(b). In regime I (lowest fields), the order parameters are close to their equilibrium values, such that the response is describable by a susceptibility perturbative expansion around the equilibrium state. Regime II (intermediate fields) is characterized by the formation of the hybrid Higgs collective mode. Regime III (highest fields) is governed by the relative phase collective mode. Figures 7(c) and 7(e) show examples of the order-parameter dynamics in regimes II and III, respectively. The corresponding relative phase dynamics is presented in Figs. 7(d) and 7(f). The Higgs-mode oscillations observable
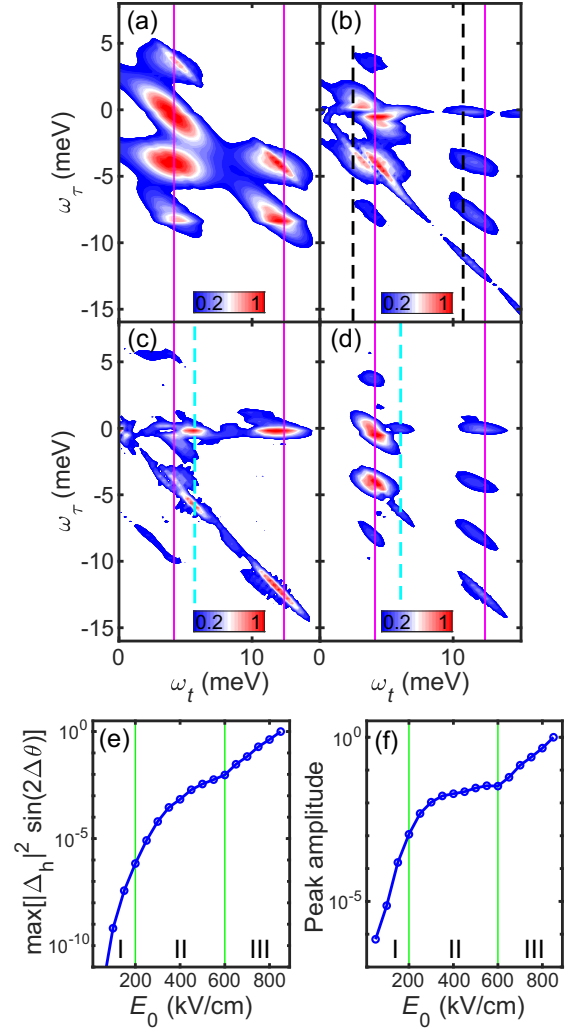

FIG. 8. Formation of bi-Higgs energy sideband in the THz-MDCS spectra of a multiband SC with strong interband coupling in the absence of persisting dynamical inversion-symmetry breaking ($\mathbf{p}_S = 0$ after the pulse). (a)–(c) Normalized THz-MDCS spectra $E_{NL}(\omega_t, \omega_\tau)$ for electric field strengths of (a) 200 kV/cm, (b) 400 kV/cm, and (c) 800 kV/cm. (d) Normalized THz-MDCS spectrum resulting from a calculation without phase-amplitude coupling, Eq. (32), for electric field strength of 800 kV/cm. Vertical dashed black lines mark $\omega_t = \omega_{H,h} \pm \omega_0$. Vertical solid magenta lines indicate $\omega_t = \omega_0$ and $3\omega_0$ while dashed cyan lines denote $\omega_t = 2\omega_{H,h} - \omega_0$. (e), (f) Correlation in the field strength dependence of the maximum of the $2|\Delta_h|^2 \sin 2\Delta\theta$ spectrum (e) and the $\omega_t = 2\omega_{H,h} - \omega_0$ sideband peaks in the THz-MDCS spectra (f). Vertical lines indicate the excitation regimes I–III.

in $|\Delta_h(t)|$ are damped in both excitation regimes. The relative phase oscillations are also weak and damped in regime II. However, they are undamped and amplified in regime III, showing a beating oscillation pattern. The observed beating oscillations of $\Delta\theta(t)$ in regime III signify the coupling between the amplitude and relative phase, now both oscillating close to the same Higgs frequency $\sim\omega_{H,h}$.

We now turn to the THz-MDCS spectra. Figures 8(a)–8(c) present example spectra in regime I [Fig. 8(a)], regime II [Fig. 8(b)], and regime III [Fig. 8(c)]. In regime I, the

THz-MDCS spectrum shows pump-probe, four-wave-mixing, and third-harmonic generation peaks similar to the weak-excitation result without interband coupling [Fig. 3(c)]. With increasing pulse-pair excitation in regime II [Fig. 8(b)], difference-frequency Raman peaks form at frequencies $\omega_t = \omega_{H,h} \pm \omega_0$ (vertical dashed black lines). Similar to the $U = 0$ result presented in Fig. 3(d), these peaks are generated by ninth-order nonlinear processes that take into account the light-induced modulation of the SC energy gap. They split from the conventional peaks located at $\omega_t = \omega_0, 3\omega_0$ (vertical solid magenta lines). Unlike in the previous two excitation regimes, however, in regime III [Fig. 8(c)], new dominant peaks emerge at a *different frequency* of $\omega_t = 2\omega_{H,h} - \omega_0$ (dashed cyan line). These peaks at *bi-Higgs frequencies* are not observable for small U (Fig. 6) or without interband interaction (Fig. 3).

We next demonstrate that the bi-Higgs-frequency sidebands observed for strong driving fields and large U are generated by parametrical driving of pseudospins by relative phase dynamics at frequency $\omega_{H,h}$ arising from the relative phase collective mode (see Sec. III). The parametrical driving of pseudospins by Eq. (25) is enhanced by the light-induced formation of the relative phase mode seen in Fig. 7(b). Several observations associate the emergence of bi-Higgs-frequency sidebands in the THz-MDCS spectra with the formation of the relative phase mode at $\omega_{H,h}$ of a light-driven nonequilibrium state absent for small U. First, we note that the bi-Higgs sideband is clearly observed in regime III, i.e., above the critical driving field threshold where the relative phase mode has formed. This result indicates that the relative phase dynamics is crucial for the formation process of the bi-Higgs-frequency sideband. Second, as demonstrated in Fig. 8(d), the THz-MDCS peaks at $\omega_t = 2\omega_{H,h} - \omega_0$ vanish when the term $|\Delta_h|^2 \sin(2\Delta\theta)\Delta\tilde{\rho}_1^{(h)}$ in Eq. (25) is switched off. This term causes the time-dependent transverse coupling of the pseudospin components driven by $\Delta\theta(t)$. This coupling is enhanced by the strong modulation of the superfluid density, which is characterized by the light-induced changes in $|\Delta_h|^2$. Expansion of this coupling in terms of $\Delta\theta$ gives

$$2|\Delta_h|^2 \sin 2\Delta\theta(t)\Delta\rho_1^{(h)} = 4|\Delta_h|^2 \Delta\theta \Delta\tilde{\rho}_1^{(h)} + O[(\Delta\theta)^2], \tag{32}$$

to lowest order in $\Delta\theta$. In regime III, long-lived relative phase oscillations at frequency $\omega_{H,h}$ arise from the formation of the underdamped relative phase mode. As discussed in Sec. IV A, the $\Delta\tilde{\rho}_1^{(\nu)}$ dynamics is dominated by quasiparticle excitations also at frequency $\sim\omega_{H,h}$. Therefore, the transverse coupling term (32) drives the nonlinear coupled parametric oscillator equations (21) with the bi-Higgs frequency $\sim 2\omega_{H,h}$. Based on Eq. (31), we then find that the the transverse coupling of pseudospin components manifests itself via bi-Higgs-frequency sideband peaks located at $(2\omega_{H,h} - \omega_0, 0)$ and $(2\omega_{H,h} - \omega_0, -2\omega_{H,h} + \omega_0)$. These Floquet-type sidebands are clearly observed as distinct peaks in our numerical results. They are generated by ninth-order nonlinear processes $2\omega_{A,B} - 2\omega_{A,B} + 2\omega_{H,h}^{B,A} - \omega_{B,A}$. Third, to provide further evidence for the proposed physical picture, we show in Fig. 8(e) the field dependence of the maximum of the $2|\Delta_h|^2 \sin 2\Delta\theta$ spectrum [amplitude of the driving term (32)] while the field
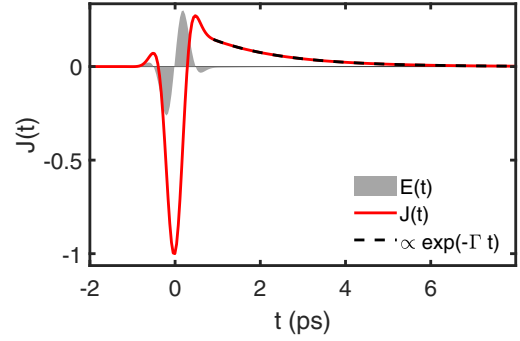

FIG. 9. Time dependence of the current density $J(t)$ (red curve) when electromagnetic propagation effects are taken into account in a thin-film geometry with film thickness $d = 20$ nm. By comparing the time dependence of $J(t)$ with that of the THz laser pulse (shaded area), it is clear that the current lasts longer than the pulse duration. It decays exponentially after the pulse, with the dashed line showing the radiative damping with decay time ~ 1.7 ps.

dependence of the bi-Higgs-frequency sideband peak in the THz-MDCS spectra at $\omega_t = 2\omega_{H,h} - \omega_0$ is plotted in Fig. 8(f). Both quantities are smaller than 10^{-3} in regime I. In regime II, where the relative phase mode redshifts towards the Higgs mode energy, both quantities increase up to an amplitude of about 10^{-2}. Specifically, this increase flattens close to the transition from regime II to regime III. In regime III, however, where the relative phase mode is located close to the Higgs mode energy, both quantities grow strong compared to the intensity range of $[400, 600]$ kV/cm in regime II. This strong increase of both quantities indicates that the bi-Higgs frequency signals results from the long-lived dynamics of the order-parameter relative phase.

In summary, a comparison of Figs. 3 ($U = 0$), 6 ($|U| < 1$), and 8 ($|U| > 1$) demonstrates how the changes in the spectral profile of THz-MDCS with increasing pulse-pair driving reflects the properties of the SC nonequilibrium states for different interband interactions in the case of zero Cooper-pair momentum after the pulse. In the next section, we show how the dynamical breaking of inversion symmetry achieved via electromagnetic propagation effects changes the above spectral profiles in significant ways that allow the direct observation of the nonequilibrium state collective modes without applying any symmetry-breaking static fields.

V. THz-MDCS WITH LIGHT-INDUCED DYNAMICAL INVERSION-SYMMETRY BREAKING

So far, we have presented results without including the electromagnetic propagation effects. The latter effects change the effective driving field from the laser field considered in the previous sections, which results in a current that lasts much longer than the laser pulse (Fig. 9). This current leads to persistent light-induced inversion-symmetry breaking, which has significant effects on the THz-MDCS spectral peaks that can be directly observed experimentally. To identify the corresponding spectral features, we consider the full self-consistent solution of the SC Bloch equations, which takes into account light-induced finite-momentum Cooper pairing persisting well after the pulse.
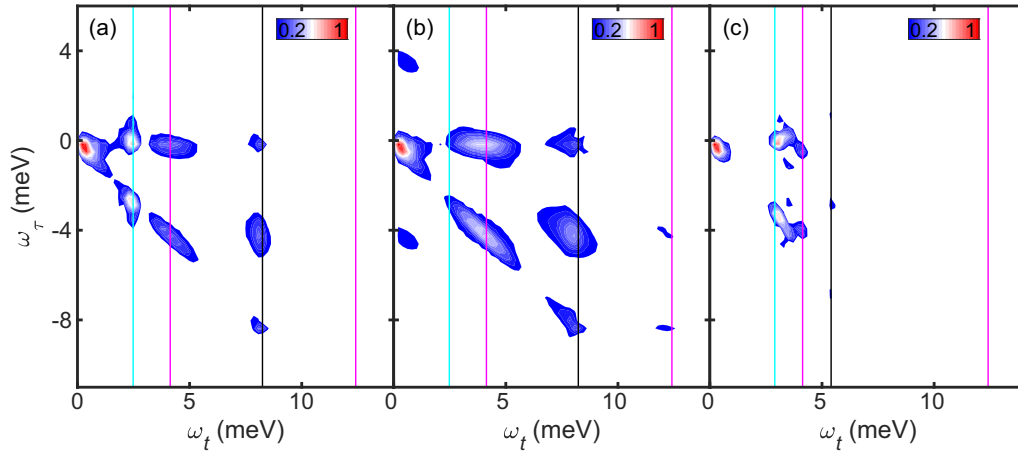
FIG. 10. Sensing of the Higgs and Leggett collective modes and THz dynamical inversion-symmetry breaking in the THz-MDCS spectra for weak interband interaction $U = 0.01$ as in Fig. 6. (a) Normalized THz-MDCS spectrum $E_{\mathrm{NL}}(\omega_t, \omega_\tau)$ resulting from a simulation with light-wave electromagnetic propagation effects for an electric field strength of 200 kV/cm. (b), (c) Normalized $E_{\mathrm{NL}}(\omega_t, \omega_\tau)$ for a calculation with propagation effects but without Leggett collective mode effects and a calculation with propagation effects but without Higgs collective mode effects. Vertical magenta lines denote $\omega_t = \omega_0$ and $\omega_t = 3\omega_0$. The Leggett (Higgs) mode signals at $\omega_t = \omega_{\mathrm{L}}$ ($\omega_t = \omega_{\mathrm{H,h}}$) are indicated with a solid cyan (black) line.

A. Dominant intraband interaction

For one-band SCs, Ref. [10] showed that photogeneration of a DC current that persists well after the pulse leads to Higgs collective mode distinct peaks in the THz-MDCS spectra. The latter peaks are generated by high-order difference-frequency Raman processes [28], with inversion-symmetry breaking achieved dynamically via light-wave electromagnetic propagation. We have already shown that such photogenerated DC supercurrent yields high-harmonic generation at equilibrium-symmetry forbidden frequencies, and also leads to gapless superconductivity [28,36,46]. Here, we extend these results to multiband SCs and demonstrate direct sensing with THz-MDCS of Leggett and Higgs collective excitations of strongly driven states. While the Higgs mode can also be observed for weak fields if a DC external current is applied to break the equilibrium inversion symmetry, with increasing field, it is hidden by the quasiparticle continua in conventional one-dimensional spectra [11]. As a result, we cannot discern the collective modes of the strongly driven nonequilibrium state in this way, unlike for THz-MDCS.

To take into account the light-wave electromagnetic propagation effects, we solved self-consistently the Bloch equations (6) together with Eq. (15) in the homogeneous system with penetration depth larger than the film thickness. Figure 10(a) presents an example of the THz-MDCS spectrum obtained with this calculation for weak interband interaction $U = 0.01$ similar to Fig. 6. While we used the same field strength and interband interaction strength as in Fig. 6(b), the THz-MDCS of Fig. 10(a) displays a different spectral profile. In particular, the finite-momentum Cooper pairing results in a THz-MDCS spectrum showing distinct peaks at the Leggett mode energy ($\omega_t = \omega_{\mathrm{L}}$, solid cyan line) and at the Higgs mode energy ($\omega_t = \omega_{\mathrm{H,h}}$, solid black line). These sharp peaks replace the broad line shape of Fig. 6(b). To verify that they are indeed generated by Leggett and Higgs collective effects, rather than by quasiparticle excitations, we show in

Figs. 10(b) and 10(c) the corresponding results of our simulations without the Leggett and Higgs collective contributions to Eq. (21), respectively. In particular, the peaks at $\omega_t = \omega_{\mathrm{L}}$ vanish without the phase mode collective effects in Eq. (21), while the signals at $\omega_t = \omega_{\mathrm{H,h}}$ are suppressed without the Higgs collective contribution. These peaks at the collective mode frequencies become observable due to light-induced symmetry breaking as in Fig. 9 and replace the sidebands at $\omega_{H,h} \pm \omega_0$ and $\omega_{\mathrm{L}} \pm \omega_0$ observed without persistent Cooper-pair momentum in Fig. 6(b). This result demonstrates that the light-induced dynamical inversion-symmetry breaking allows THz-MDCS signals to be used for sensing the collective modes of multiband superconductor nonequilibrium states under strong THz excitation.

It is important to note that the Leggett and Higgs mode peaks in the THz-MDCS spectra are generated by high-order coherent nonlinear processes. These high-order nonlinearities include difference-frequency coherent Raman processes leading to coherent photogeneration of a DC supercurrent and quantum quench of the energy gap during light field oscillation cycles. In particular, the observed collective mode peaks characterize a superfluid state with a finite Cooper-pair momentum $\mathbf{p}_{\mathrm{S}}$ that includes both oscillating and static $\omega = 0$ components. The finite-momentum Cooper pairing is in addition to the ω_0 oscillatory component determined by the laser frequency. In its presence, the sum- and difference-frequency Raman processes that led to the peaks at $\omega_t = \omega_{\mathrm{H,h}} \pm \omega_0$ and $\omega_t = \omega_0 \pm \omega_{\mathrm{L}}$ in the THz-MDCS spectra of Fig. 6 now generate new peaks at $\omega_t = \omega_{\mathrm{L}}$ and $\omega_{\mathrm{H,h}}$. These new peaks reflect the light-induced inversion-symmetry breaking that persists after the pulse in a moving condensate state. To explain the THz-MDCS experiments [11], an important difference from semiconductors in the strong excitation regime is that we must consider nonlinear processes around a light-driven nonequilibrium SC state that differs from the equilibrium state. As a result, THz-MDCS can
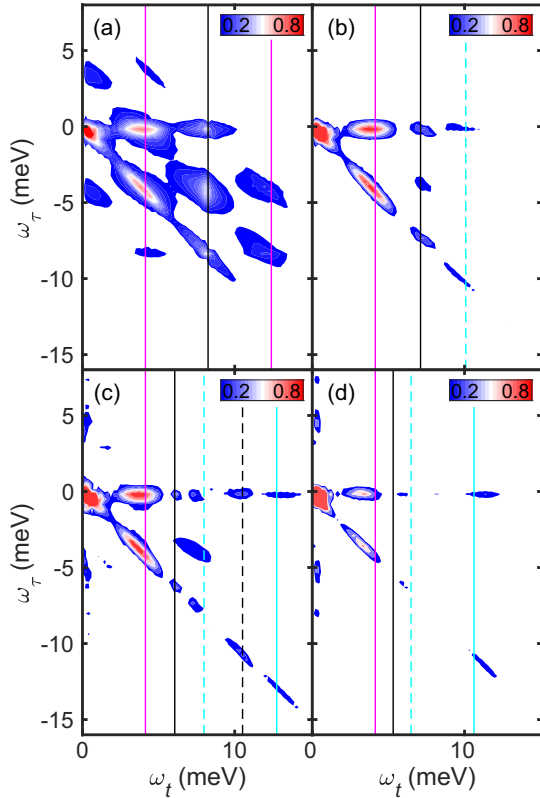
FIG. 11. Transition from a nonequilibrium state characterized by a hybrid Higgs amplitude collective mode to a nonequilibrium state determined by a relative phase mode. Normalized THz-MDCS spectra $E_{NL}(\omega_t, \omega_\tau)$ resulting from a simulation with light-wave electromagnetic propagation effects for electric field strength of (a) 150 kV/cm, (b) 400 kV/cm, (c) 650 kV/cm, and (d) 900 kV/cm. Vertical magenta lines indicate $\omega_t = \omega_0$ and $3\omega_0$. The signals at $\omega_t = \omega_{H,h}$ and $2\omega_{H,h}$ are denoted by vertical solid black and cyan lines, respectively. The signals at $\omega_t = \omega_{H,h} + \omega_0$ and $2\omega_{H,h} - \omega_0$ are marked by vertical dashed black and cyan lines, respectively.

be used to observe the excitations of nonequilibrium superconductor states controlled by a pulse pair. More generally, unlike for the rigid properties of conventional materials determined by band structure, the soft properties of quantum materials can be coherently modified by light, which must be considered when interpreting their nonlinear response [58,59].

B. Dominant interband interaction

The light-induced transition for strong $U = 2$ from a nonequilibrium state characterized by the Higgs mode to a nonequilibrium state determined by the relative phase of Sec. IV B is directly observable in the THz-MDCS spectra when dynamical inversion-symmetry breaking is induced by the electromagnetic propagation. Figure 11 shows examples of the calculated THz-MDCS spectra in regime I [Fig. 11(a)], regime II [Fig. 11(b)], at the transition from regime II to regime III [Fig. 11(c)], and in regime III [Fig. 11(d)]. In regime I (lowest fields), the THz-MDCS spectrum shows strong peaks at the Higgs mode frequency $\omega_t = \omega_{H,h}$. These peaks measure directly the Higgs amplitude

collective mode (black solid line) as discussed in Sec. V A. Unlike for conventional one-dimensional spectroscopies, the Higgs frequency peaks are well separated from the pump-probe, four-wave-mixing, and third-harmonic generation peaks (vertical magenta lines) in 2D frequency space. By providing a high-resolution two-dimensional visualization of the nonequilibrium SC state, THz-MDCS allows to directly detect the collective modes of the nonequilibrium driven states. In regime II [intermediate fields, Fig. 11(b)], a relative phase starts to form from the Higgs and hybrid Higgs amplitude modes. The bi-Higgs-frequency sidebands at $\omega_t = 2\omega_{H,h} - \omega_0$ (dashed cyan line) then start to emerge slightly above the Higgs mode signals at $\omega_t = \omega_{H,h}$. At the transition from regime II to regime III [Fig. 11(c)], the THz-MDCS spectrum shows both Higgs (dashed black line) and bi-Higgs-frequency satellites (dashed cyan line), at $\omega_t = \omega_{H,h} + \omega_0$ and $\omega_t = 2\omega_{H,h} - \omega_0$, in addition to the Higgs-mode signals at $\omega_t = \omega_{H,h}$ (vertical solid black line). Most importantly, new signals now emerge at the bi-Higgs frequency $\omega_t = 2\omega_{H,h}$ (vertical solid cyan line), which represent a direct observation of the relative phase mode. These bi-Higgs-frequency peaks become observable due to persisting inversion-symmetry breaking by photogenerated DC supercurrent and finite-momentum Cooper pairing. The bi-Higgs-frequency signals dominate over the Higgs peaks in regime III [higher fields, Fig. 11(d)]. In this excitation regime, the strong nonlinear increase of the $2|\Delta_h|^2 \sin 2\Delta\theta$ spectral peak in Fig. 8(e) exceeds the corresponding light-induced DC current contribution. As a result, the THz-MDCS signals generated by the relative phase collective mode at $\omega_t = 2\omega_{H,h}$ dominate over the Higgs collective mode signals at $\omega_t = \omega_{H,h}$. The observed change in THz-MDCS spectral profile reflects the transition from a nonequilibrium state characterized by the hybrid Higgs collective mode to a nonequilibrium state determined by the relative phase collective mode, observed experimentally in Ref. [11]. The agreement between experiment and theory indicates that long-lived, light-accelerated moving condensate driven states can be sensed and controlled with super-resolution by THz MDCS since it provides the necessary resolution to observe higher-order correlations and corresponding nonlinear responses in contrast to one-dimensional coherent spectroscopy where multiple different nonlinear processes contribute to the same frequencies.

VI. SUMMARY

In this paper, we have provided a detailed microscopic theory allowing us to propose that THz-MDCS experiments on multiband superconductors with varying interband couplings can be used to both drive different nonequilibrium SC states and characterize them uniquely by measuring their collective modes. For this purpose, we first extended the gauge-invariant density matrix approach of Refs. [10,28] to the multiband case. The resulting superconductor Maxwell-Bloch equations describe the nonlinear dynamics of light-wave acceleration of different finite-momentum Cooper-pair condensate states that live after the pulse. We have shown that these nonequilibrium states are characterized by quasiparticle excitations and collective amplitude and phase modes that differ from those of the equilibrium SC state. We have pointed

out smoking-gun signals in the THz-MDCS spectra that signify the transition to such light-driven SC states. For this, we have derived nonlinearly coupled Anderson pseudospin oscillator equations of motion. These coupled oscillators are driven by the competition between the time-dependent superfluid momentum and the order-parameter relative phase. This light-controlled competition depends critically on the interband interaction strength. The superfluid momentum is controlled by both the applied THz laser field and by light-wave electromagnetic propagation effects. As a result, the effective field pulse that drives the superconductor differs from the applied laser pulse. The spectrum of this effective driving pulse can include an inversion-symmetry-breaking DC component, which can lead to formation of a DC supercurrent and long-lived finite-momentum Cooper pairing. On the other hand, a transverse driving of the Anderson pseudospin oscillators by the relative phase mode oscillations can dominate over analogous effects driven by the Cooper-pair momentum for multiband superconductors with strong interband coupling. Here, unlike for the strongly damped Leggett collective mode of the equilibrium state, which lies within the quasiparticle continuum, the relative phase collective mode has frequency close to the SC energy gap in the case of strong interband interaction.

We have applied the presented theory in the homogeneous limit to calculate the THz-MDCS spectra for different interband-to-intraband interaction ratios and for weak to strong pulse-pair excitation. The presented results demonstrate a direct ultrafast visualization of THz-driven moving condensate states by using THz-MDCS. In particular, in the case of small interband interactions, the THz-MDCS spectra show a transition from traditional third-order nonlinear signals, i.e., pump-probe, four-wave-mixing, and third-harmonic generation signals, to harmonic sidebands that split from the conventional signals due to the quantum quench of the superconductor excitation energy gap as a result of Raman difference-frequency nonlinear processes during cycles of laser field oscillations. With increasing driving field, ninth-order nonlinear signals (with respect to the equilibrium state) emerge as a result of quasiparticle excitations of the nonequilibrium state assisted by difference-frequency Raman processes. For intraband interaction exceeding the interband coupling, the Leggett phase mode lies within the energy gap and leads to the formation of harmonic sidebands around the pump-probe peaks. We have shown that the photoexcitation of a long-lived DC supercurrent via light-wave propagation inside a thin superconducting film, neglected in previous works, allows the Leggett and Higgs collective modes to be simultaneously detected as distinct peaks in the THz-MDCS spectra.

We also studied the case of multiband superconductors with interband coupling exceeding the intraband pairing interaction. The drastic change of the THz-MDCS spectral profile in this case reveals a transition from a nonequilibrium state characterized by a hybrid Higgs amplitude collective mode to a state with a relative phase collective mode. The latter strongly driven state manifests itself directly in the THz-MDCS spectra via the formation of Floquet-type sidebands at bi-Higgs frequencies. We have demonstrated that such new bi-Higgs-frequency signals are generated by ninth-order nonlinear processes (with respect to the equilibrium state) and arise from the interaction of the relative phase collective mode with quasiparticle excitations, both at the Higgs mode energy. The relative phase collective mode forms above critical driving when the relative phase Leggett mode, which close to equilibrium is located within the quasiparticle continuum, has shifted towards the low-energy Higgs mode. The formed relative phase collective mode parametrically drives pseudospin oscillators. This light-induced effect is enhanced by the strong modulation of the superfluid density, such that the relative phase mode driving of the pseudospin oscillators exceeds their superfluid momentum driving at elevated effective fields. As a result, bi-Higgs-frequency signals exceed the harmonic Higgs peaks in the THz-MDCS spectra, but only in the presence of photogenerated DC supercurrent and persistent finite-momentum Cooper pairing.

The theoretical approach presented here can be extended to study the THz-driven nonequilibrium dynamics in systems with SC order parameter coupled to spin or charge order, as in iron-based and topological superconductors. There, THz-MDCS could be used to detect new nonequilibrium states and to identify the SC order-parameter equilibrium symmetry. Specifically, we expect that superconductors with d-wave order-parameter symmetry will show a very different THz-MDCS spectrum than s-wave superconductors due to the presence of gap nodes. In this context, it will be also interesting to see how the real and imaginary parts of the THz-MDCS spectra change as a function of interband-interaction strength and field strength for different SC order-parameter equilibrium symmetries. Our theoretical approach can also be applied to study more complex amplitude modes of the SC order parameter, such as, e.g., solitonlike states [60,61]. The latter nonequilibrium states are characterized by persisting oscillations of the SC order parameter with unchanged amplitude and frequency [28,62]. These states emerge above critical THz field strengths and are driven by Rabi-Higgs flopping, to be discussed elsewhere. Such nonequilibrium state modes are expected to show up as unique distinct peaks in the THz-MDCS spectra. Similarly, THz-MDCS can be used to identify the role of coherent interactions or correlations between many collective modes of the nonequilibrium states. Moreover, the THz-MDCS approach and understanding presented here can be readily applied to explore the intriguing realm of quantum materials featuring topological [63–67], magnetic [68,69], and charge density wave properties [70].

In summary, by using our developed theory to analyze THz-MDCS experiments and drive quantum nonlinear dynamics with strong phase-locked pulse pairs, it is possible to reconstruct nonequilibrium driven quantum states with super-resolution in a broad range of interesting quantum systems, thus achieving quantum tomography of nonequilibrium light-driven quantum states.

APPENDIX A: GAUGE-INVARIANT DENSITY MATRIX APPROACH

In this Appendix, we extend the gauge-invariant density matrix approach of Ref. [28] to the multiband case. We first present the derivation of Hamiltonian (1). We start from the general Hamiltonian introduced by Nambu in Ref. [47] extended to the multiband case:

$$
\begin{aligned}
H = &\sum_{\nu,\alpha} \int \mathrm{d}^3\mathbf{x}\, \psi^\dagger_{\alpha,\nu}(\mathbf{x})\{\xi_\nu[\mathbf{p} - e\mathbf{A}(\mathbf{x})] + e\phi(\mathbf{x})\}\psi_{\alpha,\nu}(\mathbf{x}) \\
&- \frac{1}{2}\sum_{\alpha\beta\nu\lambda} \int \mathrm{d}^3\mathbf{x}\, \mathrm{d}^3\mathbf{x}'\, \psi^\dagger_{\alpha,\nu}(\mathbf{x})\psi^\dagger_{\beta,\lambda}(\mathbf{x}') \\
&\times V(\mathbf{x}, \mathbf{x}')\psi_{\beta,\lambda}(\mathbf{x}')\psi_{\alpha,\nu}(\mathbf{x}),
\end{aligned} \tag{A1}
$$

with Coulomb potential $V(\mathbf{x}, \mathbf{x}')$. Applying a mean-field decoupling of the interaction part of Eq. (A1) leads to

$$
\begin{aligned}
H = &\sum_{\nu,\alpha} \int \mathrm{d}^3\mathbf{x}\, \psi^\dagger_{\alpha,\nu}(\mathbf{x})\big\{\xi_\nu[\mathbf{p} - e\mathbf{A}(\mathbf{x}, t)] + e\phi(\mathbf{x}, t) \\
&+ \mu^\nu_{\mathrm{H}}(\mathbf{x})\big\}\psi_{\alpha,\nu}(\mathbf{x}) - \sum_\nu \int \mathrm{d}^3\mathbf{x}[\Delta_\nu(\mathbf{x})\psi^\dagger_{\uparrow,\nu}(\mathbf{x})\psi^\dagger_{\downarrow,\nu}(\mathbf{x}) \\
&+ \text{H.c.}] + H_{\mathrm{F}},
\end{aligned} \tag{A2}
$$

with SC order parameter $\Delta_\nu(\mathbf{x})$ and Hartree potential $\mu^\nu_{\mathrm{H}}(\mathbf{x})$ defined in Eqs. (2) and (3). Here, we have neglected interband contributions of the form $\langle \psi^\dagger_{\alpha,\nu}(\mathbf{x})\psi_{\beta,\lambda}(\mathbf{x})\rangle$ with $\nu \neq \lambda$ and replaced the Coulomb interaction $V(\mathbf{x}, \mathbf{x}')$, except in the Hartree potential, by an effective electron-electron interaction $g_{\nu,\lambda}$. The Fock term in Eq. (A2) is explicitly given by

$$
H_{\mathrm{F}} = -\sum_{\alpha,\beta,\nu} \int \mathrm{d}^3\mathbf{x}\,\langle \psi^\dagger_{\alpha,\nu}(\mathbf{x})\psi_{\beta,\nu}(\mathbf{x})\rangle g_{\nu,\nu}\psi^\dagger_{\beta,\nu}(\mathbf{x})\psi_{\alpha,\nu}(\mathbf{x}),
$$

$$
\tag{A3}
$$

which includes contributions with the same spin as well as terms with opposite spin. However, based on Refs. [37,47] it is sufficient to include only the contributions with the same spin in the Fock field (A3) to guarantee charge conservation such that Hamiltonian (A2) reduces to Eq. (1).

Hamiltonian (1) is gauge invariant under the general gauge transformation [47]

$$
\Psi_\nu(\mathbf{x}) \rightarrow e^{i\sigma_3\Lambda(\mathbf{x})/2}\Psi_\nu(\mathbf{x}) \tag{A4}
$$

when the vector potential, scalar potential, and SC order-parameter phases all transform as

$$
\mathbf{A}(\mathbf{x}) \rightarrow \mathbf{A}(\mathbf{x}) + \frac{1}{2e}\nabla\Lambda(\mathbf{x}), \quad \phi(\mathbf{x}) \rightarrow \phi(\mathbf{x}) - \frac{1}{2e}\frac{\partial}{\partial t}\Lambda(\mathbf{x}),
$$

$$
\theta_\nu(\mathbf{x}) \rightarrow \theta_\nu(\mathbf{x}) + \Lambda(\mathbf{x}). \tag{A5}
$$

In the above, $\Psi_\nu(\mathbf{x}) = (\psi_{\uparrow,\nu}(\mathbf{x}), \psi^\dagger_{\downarrow,\nu}(\mathbf{x}))^T$ is the field operator for band ν in Nambu space. Unlike for the Hamiltonian, the system's density matrix is not invariant under gauge transformation. More specifically, the diagonal block of the density matrix describing band ν, $\rho^{(\nu)}(\mathbf{x}, \mathbf{x}') = \langle \hat{\rho}^{(\nu)}(\mathbf{x}, \mathbf{x}')\rangle = \langle \Psi^\dagger_\nu(\mathbf{x})\Psi_\nu(\mathbf{x}')\rangle$, depends on the specific choice of the gauge. As an alternative, we introduce center-of-mass and relative coordinates $\mathbf{R} = (\mathbf{x} + \mathbf{x}')/2$ and $\mathbf{r} = \mathbf{x} - \mathbf{x}'$ and define the

transformed density matrix [29,30]

$$
\begin{aligned}
\tilde{\rho}^{(\nu)}(\mathbf{r}, \mathbf{R}) = &\exp\left[-ie\int_0^{\frac{1}{2}} \mathrm{d}\lambda\, \mathbf{A}(\mathbf{R} + \lambda\,\mathbf{r}, t)\cdot\mathbf{r}\,\sigma_3\right] \\
&\times \rho^{(\nu)}(\mathbf{r}, \mathbf{R})\exp\left[-ie\int_{-\frac{1}{2}}^0 \mathrm{d}\lambda\, \mathbf{A}(\mathbf{R} + \lambda\,\mathbf{r}, t)\cdot\mathbf{r}\,\sigma_3\right], \quad (A6)
\end{aligned}
$$

where $\rho^{(\nu)}(\mathbf{r}, \mathbf{R}) = \langle \Psi^\dagger_\nu(\mathbf{R} + \frac{\mathbf{r}}{2})\Psi_\nu(\mathbf{R} - \frac{\mathbf{r}}{2})\rangle$ is the Wigner function. By applying the gauge transformation (A4), we see that, unlike for the original density matrix, $\tilde{\rho}^{(\nu)}(\mathbf{r}, \mathbf{R})$ transforms as [30]

$$
\tilde{\rho}^{(\nu)}(\mathbf{r}, \mathbf{R}) \rightarrow \exp[i\sigma_3\Lambda(\mathbf{R})/2]\tilde{\rho}^{(\nu)}(\mathbf{r}, \mathbf{R})\exp[-i\sigma_3\Lambda(\mathbf{R})/2]. \tag{A7}
$$

Here, the phase $\Lambda(\mathbf{R})$ only depends on the center-of-mass coordinate and not on both coordinates $\mathbf{R}$ and $\mathbf{r}$. The latter is the case for the phase of $\rho^{(\nu)}(\mathbf{r}, \mathbf{R})$, which complicates a gauge-invariant description of the nonequilibrium dynamics of superconductors, especially in the nonlinear regime.

APPENDIX B: GAUGE-INVARIANT SPATIALLY DEPENDENT SUPERCONDUCTOR BLOCH EQUATIONS

We calculate the dynamics of the density matrix (A6) by using the Heisenberg equation of motion

$$
i\frac{\partial}{\partial t}\tilde{\rho}^{(\nu)} = \langle [\tilde{\rho}^{(\nu)}, H]\rangle. \tag{B1}
$$

Here we work with the Wigner function

$$
\tilde{\rho}^{(\nu)}(\mathbf{k}, \mathbf{R}) = \int \mathrm{d}^3\mathbf{r}\, \tilde{\rho}^{(\nu)}(\mathbf{r}, \mathbf{R})\, e^{-i\mathbf{k}\cdot\mathbf{r}} \tag{B2}
$$

rather than $\tilde{\rho}^{(\nu)}(\mathbf{r}, \mathbf{R})$, obtained by Fourier transformation with respect to the relative coordinate $\mathbf{r}$. In the case of weak order-parameter spatial dependence, we can then expand contributions to the equations of motion of the form $\Delta_\nu(\mathbf{R} + \frac{i}{2}\nabla_\mathbf{k})\tilde{\rho}^{(\nu)}(\mathbf{k}, \mathbf{R})$ by applying the gradient expansion

$$
\Delta_\nu\left(\mathbf{R} + \frac{i}{2}\nabla_\mathbf{k}\right) = \sum_{n=0}^\infty \left(\frac{i}{2}\right)^n \frac{(\nabla_\mathbf{R}\cdot\nabla_\mathbf{k})^n}{n!}\Delta_\nu(\mathbf{R}). \tag{B3}
$$

Such expansions in powers of $\nabla_\mathbf{R}\cdot\nabla_\mathbf{k}$ are most useful when the coherence length of the SC state is shorter than the spatial variation of the system. To simplify the equations of motion further, we apply the unitary transformation

$$
\tilde{\rho}^{(\nu)}(\mathbf{k}, \mathbf{R}) = e^{-i\sigma_3\theta_{\nu_0}(\mathbf{R})/2}\tilde{\rho}^{(\nu)}(\mathbf{k}, \mathbf{R})e^{i\sigma_3\theta_{\nu_0}(\mathbf{R})/2}, \tag{B4}
$$

such that the phase of the SC order parameter $\Delta_{\nu_0}(\mathbf{R})$ only appears in an effective chemical potential as demonstrated below. We thus obtain the most general gauge-invariant SC Bloch equations for multiband spatially dependent

superconductors driven by both electric and magnetic fields. These equations include the effects of a spatially dependent scalar potential or SC order-parameter phase. The exact equations of motion for the general $\tilde{\rho}^{(\nu)}(\mathbf{k}, \mathbf{R})$ are as follows:

$$
\begin{aligned}
\mathrm{i}\frac{\partial}{\partial t}\tilde{\rho}^{(\nu)}_{1,1}(\mathbf{k}, \mathbf{R}) = \Bigg[& \xi_\nu\Bigg(\mathbf{k} - \frac{\mathrm{i}}{2}\nabla_\mathbf{R} + \mathrm{i}\frac{e}{2}\sum_{n=0}^\infty\left(-\frac{1}{4}\right)^n\frac{(\nabla_\mathbf{k}\cdot\nabla_\mathbf{R})^{2n}}{(2n+1)!}\nabla_\mathbf{k}\times\mathbf{B}(\mathbf{R}) - e\sum_{n=1}^\infty 2n\left(-\frac{1}{4}\right)^n\frac{(\nabla_\mathbf{k}\cdot\nabla_\mathbf{R})^{2n-1}}{(2n+1)!}\nabla_\mathbf{k}\times\mathbf{B}(\mathbf{R})\Bigg) \\
& -\xi_\nu\Bigg(\mathbf{k} + \frac{\mathrm{i}}{2}\nabla_\mathbf{R} - \mathrm{i}\frac{e}{2}\sum_{n=0}^\infty\left(-\frac{1}{4}\right)^n\frac{(\nabla_\mathbf{k}\cdot\nabla_\mathbf{R})^{2n}}{(2n+1)!}\nabla_\mathbf{k}\times\mathbf{B}(\mathbf{R}) - e\sum_{n=1}^\infty 2n\left(-\frac{1}{4}\right)^n\frac{(\nabla_\mathbf{k}\cdot\nabla_\mathbf{R})^{2n-1}}{(2n+1)!}\nabla_\mathbf{k}\times\mathbf{B}(\mathbf{R})\Bigg) \\
& -2\sum_{n=0}^\infty\frac{\left(\frac{\mathrm{i}}{2}\right)^{2n+1}(\nabla_\mathbf{k}\cdot\nabla_\mathbf{R})^{2n+1}}{(2n+1)!}\left(\mu^\nu_\mathrm{H}(\mathbf{R}) + \mu^{\uparrow,\nu}_\mathrm{F}(\mathbf{R})\right) - \mathrm{i}e\sum_{n=0}^\infty\frac{(\nabla_\mathbf{k}\cdot\nabla_\mathbf{R})^{2n}}{(2n+1)!}\left(-\frac{1}{4}\right)^n\mathbf{E}(\mathbf{R})\cdot\nabla_\mathbf{k}\Bigg]\tilde{\rho}^{(\nu)}_{1,1}(\mathbf{k}, \mathbf{R}) \\
& +\exp\left[\frac{\mathrm{i}}{2}\nabla_\mathbf{R}\cdot\nabla_\mathbf{k}\right]|\Delta_\nu(\mathbf{R})|\exp\left[-\mathrm{i}\,\delta\theta_\nu(\mathbf{R}) - \frac{1}{2}\sum_{n=0}^\infty\frac{(\nabla_\mathbf{k}\cdot\nabla_\mathbf{R})^n}{(n+1)!}\left(\frac{\mathrm{i}}{2}\right)^n\mathbf{p}^\nu_\mathrm{S}(\mathbf{R})\cdot\nabla_\mathbf{k}\right]\tilde{\rho}^{(\nu)}_{2,1}(\mathbf{k}, \mathbf{R}) \\
& -\exp\left[-\frac{\mathrm{i}}{2}\nabla_\mathbf{R}\cdot\nabla_\mathbf{k}\right]|\Delta_\nu(\mathbf{R})|\exp\left[\mathrm{i}\,\delta\theta_\nu(\mathbf{R}) - \frac{1}{2}\sum_{n=0}^\infty\frac{(\nabla_\mathbf{k}\cdot\nabla_\mathbf{R})^n}{(n+1)!}\left(-\frac{\mathrm{i}}{2}\right)^n\mathbf{p}^\nu_\mathrm{S}(\mathbf{R})\cdot\nabla_\mathbf{k}\right]\tilde{\rho}^{(\nu)}_{1,2}(\mathbf{k}, \mathbf{R}), \qquad \text{(B5)}
\end{aligned}
$$

$$
\begin{aligned}
\mathrm{i}\frac{\partial}{\partial t}\tilde{\rho}^{(\nu)}_{2,2}(\mathbf{k}, \mathbf{R}) = \Bigg[& \xi_\nu\Bigg(-\mathbf{k} - \frac{\mathrm{i}}{2}\nabla_\mathbf{R} - \mathrm{i}\frac{e}{2}\sum_{n=0}^\infty\left(-\frac{1}{4}\right)^n\frac{(\nabla_\mathbf{k}\cdot\nabla_\mathbf{R})^{2n}}{(2n+1)!}\nabla_\mathbf{k}\times\mathbf{B}(\mathbf{R}) + e\sum_{n=1}^\infty 2n\left(-\frac{1}{4}\right)^n\frac{(\nabla_\mathbf{k}\cdot\nabla_\mathbf{R})^{2n-1}}{(2n+1)!}\nabla_\mathbf{k}\times\mathbf{B}(\mathbf{R})\Bigg) \\
& -\xi_\nu\Bigg(-\mathbf{k} + \frac{\mathrm{i}}{2}\nabla_\mathbf{R} + \mathrm{i}\frac{e}{2}\sum_{n=0}^\infty\left(-\frac{1}{4}\right)^n\frac{(\nabla_\mathbf{k}\cdot\nabla_\mathbf{R})^{2n}}{(2n+1)!}\nabla_\mathbf{k}\times\mathbf{B}(\mathbf{R}) + e\sum_{n=1}^\infty 2n\left(-\frac{1}{4}\right)^n\frac{(\nabla_\mathbf{k}\cdot\nabla_\mathbf{R})^{2n-1}}{(2n+1)!}\nabla_\mathbf{k}\times\mathbf{B}(\mathbf{R})\Bigg) \\
& +2\sum_{n=0}^\infty\frac{\left(\frac{\mathrm{i}}{2}\right)^{2n+1}(\nabla_\mathbf{k}\cdot\nabla_\mathbf{R})^{2n+1}}{(2n+1)!}\left(\mu^\nu_\mathrm{H}(\mathbf{R}) + \mu^{\downarrow,\nu}_\mathrm{F}(\mathbf{R})\right) + \mathrm{i}e\sum_{n=0}^\infty\frac{(\nabla_\mathbf{k}\cdot\nabla_\mathbf{R})^{2n}}{(2n+1)!}\left(-\frac{1}{4}\right)^n\mathbf{E}(\mathbf{R})\cdot\nabla_\mathbf{k}\Bigg]\tilde{\rho}^{(\nu)}_{2,2}(\mathbf{k}, \mathbf{R}) \\
& -\exp\left[-\frac{\mathrm{i}}{2}\nabla_\mathbf{R}\cdot\nabla_\mathbf{k}\right]|\Delta_\nu(\mathbf{R})|\exp\left[-\mathrm{i}\,\delta\theta_\nu(\mathbf{R}) + \frac{1}{2}\sum_{n=0}^\infty\frac{(\nabla_\mathbf{k}\cdot\nabla_\mathbf{R})^n}{(n+1)!}\left(-\frac{\mathrm{i}}{2}\right)^n\mathbf{p}^\nu_\mathrm{S}(\mathbf{R})\cdot\nabla_\mathbf{k}\right]\tilde{\rho}^{(\nu)}_{2,1}(\mathbf{k}, \mathbf{R}) \\
& +\exp\left[\frac{\mathrm{i}}{2}\nabla_\mathbf{R}\cdot\nabla_\mathbf{k}\right]|\Delta_\nu(\mathbf{R})|\exp\left[\mathrm{i}\,\delta\theta_\nu(\mathbf{R}) + \frac{1}{2}\sum_{n=0}^\infty\frac{(\nabla_\mathbf{k}\cdot\nabla_\mathbf{R})^n}{(n+1)!}\left(\frac{\mathrm{i}}{2}\right)^n\mathbf{p}^\nu_\mathrm{S}(\mathbf{R})\cdot\nabla_\mathbf{k}\right]\tilde{\rho}^{(\nu)}_{1,2}(\mathbf{k}, \mathbf{R}), \qquad \text{(B6)}
\end{aligned}
$$

$$
\begin{aligned}
\mathrm{i}\frac{\partial}{\partial t}\tilde{\rho}^{(\nu)}_{1,2}(\mathbf{k}, \mathbf{R}) = \Bigg[& -\xi_\nu\Bigg(\mathbf{k} + \frac{\mathrm{i}}{2}\nabla_\mathbf{R} - e\sum_{n=0}^\infty(2n+1)\left(\frac{\mathrm{i}}{2}\right)^{2n+1}\frac{(\nabla_\mathbf{k}\cdot\nabla_\mathbf{R})^{2n}}{(2n+2)!}\nabla_\mathbf{k}\times\mathbf{B}(\mathbf{R}) \\
& -\mathrm{i}\frac{e}{2}\sum_{n=0}^\infty\left(\frac{\mathrm{i}}{2}\right)^{2n+1}\frac{(\nabla_\mathbf{k}\cdot\nabla_\mathbf{R})^{2n+1}}{(2n+2)!}\nabla_\mathbf{k}\times\mathbf{B}(\mathbf{R}) - \mathbf{p}^{\nu_0}_\mathrm{S}(\mathbf{R})/2\Bigg) \\
& -\xi_\nu\Bigg(-\mathbf{k} + \frac{\mathrm{i}}{2}\nabla_\mathbf{R} + e\sum_{n=0}^\infty(2n+1)\left(\frac{\mathrm{i}}{2}\right)^{2n+1}\frac{(\nabla_\mathbf{k}\cdot\nabla_\mathbf{R})^{2n}}{(2n+2)!}\nabla_\mathbf{k}\times\mathbf{B}(\mathbf{R}) \\
& +\mathrm{i}\frac{e}{2}\sum_{n=0}^\infty\left(\frac{\mathrm{i}}{2}\right)^{2n+1}\frac{(\nabla_\mathbf{k}\cdot\nabla_\mathbf{R})^{2n+1}}{(2n+2)!}\nabla_\mathbf{k}\times\mathbf{B}(\mathbf{R}) - \mathbf{p}^{\nu_0}_\mathrm{S}(\mathbf{R})/2\Bigg) - 2\mu_\mathrm{eff}(\mathbf{R}) \\
& -2\sum_{n=0}^\infty\frac{\left(\frac{\mathrm{i}}{2}\right)^{2n}(\nabla_\mathbf{k}\cdot\nabla_\mathbf{R})^{2n}}{(2n)!}\mu^\nu_\mathrm{H}(\mathbf{R}) - \sum_{n=0}^\infty\frac{\left(-\frac{\mathrm{i}}{2}\right)^n(\nabla_\mathbf{k}\cdot\nabla_\mathbf{R})^n}{n!}\left(\mu^{\downarrow,\nu}_\mathrm{F}(\mathbf{R}) + (-1)^n\mu^{\uparrow,\nu}_\mathrm{F}(\mathbf{R})\right) \\
& -\mathrm{i}e\sum_{n=0}^\infty\frac{(\nabla_\mathbf{k}\cdot\nabla_\mathbf{R})^{2n+1}}{(2n+2)!}\left(\frac{\mathrm{i}}{2}\right)^{2n+1}\mathbf{E}(\mathbf{R})\cdot\nabla_\mathbf{k}\Bigg]\tilde{\rho}^{(\nu)}_{1,2}(\mathbf{k}, \mathbf{R})
\end{aligned}
$$

$$+ \exp\left[\frac{i}{2}\boldsymbol{\nabla}_{\mathbf{R}} \cdot \boldsymbol{\nabla}_{\mathbf{k}}\right]|\Delta_\nu(\mathbf{R})|\exp\left[-i\,\delta\theta_\nu(\mathbf{R}) - \frac{1}{2}\sum_{n=0}^{\infty}\frac{(\boldsymbol{\nabla}_{\mathbf{k}} \cdot \boldsymbol{\nabla}_{\mathbf{R}})^n}{(n+1)!}\left(\frac{i}{2}\right)^n \mathbf{p}_S^\nu(\mathbf{R}) \cdot \boldsymbol{\nabla}_{\mathbf{k}}\right]\tilde{\rho}_{2,2}^{(\nu)}(\mathbf{k}, \mathbf{R})$$

$$- \exp\left[-\frac{i}{2}\boldsymbol{\nabla}_{\mathbf{R}} \cdot \boldsymbol{\nabla}_{\mathbf{k}}\right]|\Delta_\nu(\mathbf{R})|\exp\left[-i\,\delta\theta_\nu(\mathbf{R}) + \frac{1}{2}\sum_{n=0}^{\infty}\frac{(\boldsymbol{\nabla}_{\mathbf{k}} \cdot \boldsymbol{\nabla}_{\mathbf{R}})^n}{(n+1)!}\left(-\frac{i}{2}\right)^n \mathbf{p}_S^\nu(\mathbf{R}) \cdot \boldsymbol{\nabla}_{\mathbf{k}}\right]\tilde{\rho}_{1,1}^{(\nu)}(\mathbf{k}, \mathbf{R}). \tag{B7}$$

These full spatially dependent equations of motion do not contain the electromagnetic potentials. They only contain the gauge-invariant superfluid momentum and effective chemical potential, which are given by

$$\mathbf{p}_S^\nu(\mathbf{R}) = \boldsymbol{\nabla}_{\mathbf{R}}\theta_\nu(\mathbf{R}) - 2e\mathbf{A}(\mathbf{R}),$$

$$\mu_{\mathrm{eff}}(\mathbf{R}) = e\,\phi(\mathbf{R}) + \frac{1}{2}\frac{\partial}{\partial t}\theta_{\nu_0}(\mathbf{R}), \tag{B8}$$

as well as the electric and magnetic fields

$$\mathbf{E}(\mathbf{R}) = -\boldsymbol{\nabla}_{\mathbf{R}}\phi(\mathbf{R}) - \frac{\partial}{\partial t}\mathbf{A}(\mathbf{R}), \quad \mathbf{B}(\mathbf{R}) = \boldsymbol{\nabla}_{\mathbf{R}} \times \mathbf{A}(\mathbf{R}). \tag{B9}$$

The Higgs mode is determined by amplitude fluctuations of the SC order parameters in different bands. The latter amplitudes are expressed as

$$|\Delta_\nu(\mathbf{R})| = -\sum_{\lambda, \mathbf{k}} g_{\nu,\lambda}\exp\left[-i\delta_\lambda(\mathbf{R}) - \sum_{n=0}^{\infty}\left(\frac{i}{2}\right)^{2n+1}\frac{(\boldsymbol{\nabla}_{\mathbf{k}} \cdot \boldsymbol{\nabla}_{\mathbf{R}})^{2n+1}}{(2n+2)!}\mathbf{p}_s^{\nu_0}(\mathbf{R}) \cdot \boldsymbol{\nabla}_{\mathbf{k}}\right]\tilde{\rho}_{2,1}^{(\lambda)}(\mathbf{k}, \mathbf{R}). \tag{B10}$$

The Leggett mode corresponds to fluctuations of the phase difference between different order parameters,

$$\delta\theta_\nu(\mathbf{R}) = \theta_{\nu_0}(\mathbf{R}) - \theta_\nu(\mathbf{R}). \tag{B11}$$

The center-of-mass acceleration of the Cooper-pair condensate, determined by the electric and magnetic fields in the kinetic contributions of the equations of motion (B5)–(B7), is described by

$$\frac{\partial}{\partial t}\mathbf{p}_S^\nu(\mathbf{R}) = 2\boldsymbol{\nabla}_{\mathbf{R}}\mu_{\mathrm{eff}}(\mathbf{R}) + 2e\,\mathbf{E}(\mathbf{R}). \tag{B12}$$

This light-induced Cooper-pair total momentum breaks the equilibrium inversion symmetry. The Fock contributions to the gauge-invariant equations of motion are given by

$$\mu_F^{\uparrow,\nu}(\mathbf{R}) = -g_{\nu,\nu}\sum_{\mathbf{k}}\exp\left[-\frac{1}{2}\sum_{n=0}^{\infty}\left(\frac{i}{2}\right)^{2n}\frac{(\boldsymbol{\nabla}_{\mathbf{k}} \cdot \boldsymbol{\nabla}_{\mathbf{R}})^{2n}}{(2n+1)!}\mathbf{p}_s^{\nu_0}(\mathbf{R}) \cdot \boldsymbol{\nabla}_{\mathbf{k}}\right]\tilde{\rho}_{1,1}^{(\nu)}(\mathbf{k}, \mathbf{R}),$$

$$\mu_F^{\downarrow,\nu}(\mathbf{R}) = -g_{\nu,\nu}\sum_{\mathbf{k}}\left\{1 - \exp\left[\frac{1}{2}\sum_{n=0}^{\infty}\left(\frac{i}{2}\right)^{2n}\frac{(\boldsymbol{\nabla}_{\mathbf{k}} \cdot \boldsymbol{\nabla}_{\mathbf{R}})^{2n}}{(2n+1)!}\mathbf{p}_s^{\nu_0}(\mathbf{R}) \cdot \boldsymbol{\nabla}_{\mathbf{k}}\right]\tilde{\rho}_{2,2}^{(\nu)}(\mathbf{k}, \mathbf{R})\right\}. \tag{B13}$$

These Fock contributions ensure charge conservation of the SC system: the gauge-invariant current density

$$\mathbf{J}(\mathbf{R}) = \frac{e}{V}\sum_{\lambda, \mathbf{k}}\boldsymbol{\nabla}_{\mathbf{k}}\xi_\nu(\mathbf{k})\left[\tilde{\rho}_{1,1}^{(\nu)}(\mathbf{k}, \mathbf{R}) + \tilde{\rho}_{2,2}^{(\nu)}(\mathbf{k}, \mathbf{R})\right], \tag{B14}$$

and electron density

$$n(\mathbf{R}) = \frac{1}{V}\sum_{\lambda, \mathbf{k}}\left[1 + \tilde{\rho}_{1,1}^{(\nu)}(\mathbf{k}, \mathbf{R}) - \tilde{\rho}_{2,2}^{(\nu)}(\mathbf{k}, \mathbf{R})\right] \tag{B15}$$

satisfy the continuity equation

$$e\frac{\partial}{\partial t}n(\mathbf{R}) + \boldsymbol{\nabla}_{\mathbf{R}} \cdot \mathbf{J}(\mathbf{R}) = 0. \tag{B16}$$

This continuity and charge conservation equation directly follows from the equations of motion (B5)–(B7).

We can simplify the full equations of motion by neglecting contributions of the form $(\boldsymbol{\nabla}_{\mathbf{k}} \cdot \boldsymbol{\nabla}_{\mathbf{R}})^n[\mathbf{p}_s^\nu(\mathbf{R}) \cdot \boldsymbol{\nabla}_{\mathbf{k}}]$ in the above equations which is a valid approximation for strong homogeneous electric fields. We then obtain the following simplified

equations of motion for the density matrix to treat the case of spatial dependence induced by, e.g., strong disorder:

$$
\begin{aligned}
\mathrm{i}\frac{\partial}{\partial t}\tilde{\rho}_{1,1}^{(\nu)}(\mathbf{k},\mathbf{R}) =& \left[\xi_\nu\!\left(\mathbf{k}-\frac{\mathrm{i}}{2}\nabla_{\mathbf{R}}+\mathrm{i}\frac{e}{2}\nabla_{\mathbf{k}}\times\mathbf{B}(\mathbf{R})\right)-\xi_\nu\!\left(\mathbf{k}+\frac{\mathrm{i}}{2}\nabla_{\mathbf{R}}-\mathrm{i}\frac{e}{2}\nabla_{\mathbf{k}}\times\mathbf{B}(\mathbf{R})\right)-\mathrm{i}e\,\mathbf{E}(\mathbf{R})\cdot\nabla_{\mathbf{k}}\right.\\
&\left.-\mu_{\mathrm{H}}^{\nu}\!\left(\mathbf{R}+\frac{\mathrm{i}}{2}\nabla_{\mathbf{k}}\right)+\mu_{\mathrm{H}}^{\nu}\!\left(\mathbf{R}-\frac{\mathrm{i}}{2}\nabla_{\mathbf{k}}\right)-\mu_{\mathrm{F}}^{\uparrow,\nu}\!\left(\mathbf{R}+\frac{\mathrm{i}}{2}\nabla_{\mathbf{k}}\right)+\mu_{\mathrm{F}}^{\uparrow,\nu}\!\left(\mathbf{R}-\frac{\mathrm{i}}{2}\nabla_{\mathbf{k}}\right)\right]\tilde{\rho}_{1,1}^{(\nu)}(\mathbf{k},\mathbf{R})\\
&+\left|\Delta_\nu\!\left(\mathbf{R}+\frac{\mathrm{i}}{2}\nabla_{\mathbf{k}}\right)\right|\exp[-\mathrm{i}\,\delta\theta_\nu(\mathbf{R})]\tilde{\rho}_{2,1}^{(\nu)}(\mathbf{k}-\mathbf{p}_{\mathrm{S}}^{\nu}/2,\mathbf{R})-\left|\Delta_\nu\!\left(\mathbf{R}-\frac{\mathrm{i}}{2}\nabla_{\mathbf{k}}\right)\right|\exp[\mathrm{i}\,\delta\theta_\nu(\mathbf{R})]\tilde{\rho}_{1,2}^{(\nu)}(\mathbf{k}-\mathbf{p}_{\mathrm{S}}^{\nu}/2,\mathbf{R}),
\end{aligned}
\tag{B17}
$$

$$
\begin{aligned}
\mathrm{i}\frac{\partial}{\partial t}\tilde{\rho}_{2,2}^{(\nu)}(\mathbf{k},\mathbf{R}) =& \left[\xi_\nu\!\left(-\mathbf{k}-\frac{\mathrm{i}}{2}\nabla_{\mathbf{R}}-\mathrm{i}\frac{e}{2}\nabla_{\mathbf{k}}\times\mathbf{B}(\mathbf{R})\right)-\xi_\nu\!\left(-\mathbf{k}+\frac{\mathrm{i}}{2}\nabla_{\mathbf{R}}+\mathrm{i}\frac{e}{2}\nabla_{\mathbf{k}}\times\mathbf{B}(\mathbf{R})\right)+\mathrm{i}e\,\mathbf{E}(\mathbf{R})\cdot\nabla_{\mathbf{k}}\right.\\
&\left.+\mu_{\mathrm{H}}^{\nu}\!\left(\mathbf{R}+\frac{\mathrm{i}}{2}\nabla_{\mathbf{k}}\right)-\mu_{\mathrm{H}}^{\nu}\!\left(\mathbf{R}-\frac{\mathrm{i}}{2}\nabla_{\mathbf{k}}\right)+\mu_{\mathrm{F}}^{\downarrow,\nu}\!\left(\mathbf{R}+\frac{\mathrm{i}}{2}\nabla_{\mathbf{k}}\right)-\mu_{\mathrm{F}}^{\downarrow,\nu}\!\left(\mathbf{R}-\frac{\mathrm{i}}{2}\nabla_{\mathbf{k}}\right)\right]\tilde{\rho}_{2,2}^{(\nu)}(\mathbf{k},\mathbf{R})\\
&-\left|\Delta_\nu\!\left(\mathbf{R}-\frac{\mathrm{i}}{2}\nabla_{\mathbf{k}}\right)\right|\exp[-\mathrm{i}\,\delta\theta_\nu(\mathbf{R})]\tilde{\rho}_{2,1}^{(\nu)}(\mathbf{k}+\mathbf{p}_{\mathrm{S}}^{\nu}/2,\mathbf{R})+\left|\Delta_\nu\!\left(\mathbf{R}+\frac{\mathrm{i}}{2}\nabla_{\mathbf{k}}\right)\right|\exp[\mathrm{i}\,\delta\theta_\nu(\mathbf{R})]\tilde{\rho}_{1,2}^{(\nu)}(\mathbf{k}+\mathbf{p}_{\mathrm{S}}^{\nu}/2,\mathbf{R}),
\end{aligned}
\tag{B18}
$$

$$
\begin{aligned}
\mathrm{i}\frac{\partial}{\partial t}\tilde{\rho}_{1,2}^{(\nu)}(\mathbf{k},\mathbf{R}) =& \left[-\xi_\nu\!\left(\mathbf{k}+\frac{\mathrm{i}}{4}\nabla_{\mathbf{R}}-e\frac{\mathrm{i}}{2}\nabla_{\mathbf{k}}\times\mathbf{B}(\mathbf{R})-\mathbf{p}_{\mathrm{S}}^{\nu_0}/2\right)-\xi_\nu\!\left(-\mathbf{k}+\frac{\mathrm{i}}{2}\nabla_{\mathbf{R}}+e\frac{\mathrm{i}}{4}\nabla_{\mathbf{k}}\times\mathbf{B}(\mathbf{R})-\mathbf{p}_{\mathrm{S}}^{\nu_0}/2\right)\right.\\
&-2\mu_{\mathrm{eff}}(\mathbf{R})-\mu_{\mathrm{H}}^{\nu}\!\left(\mathbf{R}+\frac{\mathrm{i}}{2}\nabla_{\mathbf{k}}\right)-\mu_{\mathrm{H}}^{\nu}\!\left(\mathbf{R}-\frac{\mathrm{i}}{2}\nabla_{\mathbf{k}}\right)\\
&\left.-\mu_{\mathrm{F}}^{\downarrow,\nu}\!\left(\mathbf{R}-\frac{\mathrm{i}}{2}\nabla_{\mathbf{k}}\right)-\mu_{\mathrm{F}}^{\uparrow,\nu}\!\left(\mathbf{R}+\frac{\mathrm{i}}{2}\nabla_{\mathbf{k}}\right)\right]\tilde{\rho}_{1,2}^{(\nu)}(\mathbf{k},\mathbf{R})\\
&+\left|\Delta_\nu\!\left(\mathbf{R}+\frac{\mathrm{i}}{2}\nabla_{\mathbf{k}}\right)\right|\exp[-\mathrm{i}\,\delta\theta_\nu(\mathbf{R})]\tilde{\rho}_{2,2}^{(\nu)}(\mathbf{k}-\mathbf{p}_{\mathrm{S}}^{\nu}/2,\mathbf{R})\\
&-\left|\Delta_\nu\!\left(\mathbf{R}-\frac{\mathrm{i}}{2}\nabla_{\mathbf{k}}\right)\right|\exp[-\mathrm{i}\,\delta\theta_\nu(\mathbf{R})]\tilde{\rho}_{1,1}^{(\nu)}(\mathbf{k}+\mathbf{p}_{\mathrm{S}}^{\nu}/2,\mathbf{R}).
\end{aligned}
\tag{B19}
$$

When the SC system is only weakly spatially dependent, we can neglect all orders $O(\nabla_{\mathbf{k}}\cdot\nabla_{\mathbf{R}})$ and higher in the above equations. In the case of a homogeneous system, we then obtain

$$
\begin{aligned}
\mathrm{i}\frac{\partial}{\partial t}\tilde{\rho}_{1,1}^{(\nu)}(\mathbf{k}) &= -\mathrm{i}\,e\,\mathbf{E}(t)\cdot\nabla_{\mathbf{k}}\tilde{\rho}_{1,1}^{(\nu)}(\mathbf{k})-|\Delta_\nu|\bigl[e^{\mathrm{i}\,\delta\theta_\nu}\tilde{\rho}_{1,2}^{(\nu)}(\mathbf{k}-\mathbf{p}_{\mathrm{S}}/2)-e^{-\mathrm{i}\,\delta\theta_\nu}\tilde{\rho}_{2,1}^{(\nu)}(\mathbf{k}-\mathbf{p}_{\mathrm{S}}/2)\bigr],\\
\mathrm{i}\frac{\partial}{\partial t}\tilde{\rho}_{2,2}^{(\nu)}(\mathbf{k}) &= \mathrm{i}\,e\,\mathbf{E}(t)\cdot\nabla_{\mathbf{k}}\tilde{\rho}_{2,2}^{(\nu)}(\mathbf{k})+|\Delta_\nu|\bigl[e^{\mathrm{i}\,\delta\theta_\nu}\tilde{\rho}_{1,2}^{(\nu)}(\mathbf{k}+\mathbf{p}_{\mathrm{S}}/2)-e^{-\mathrm{i}\,\delta\theta_\nu}\tilde{\rho}_{2,1}^{(\nu)}(\mathbf{k}+\mathbf{p}_{\mathrm{S}}/2)\bigr],\\
\mathrm{i}\frac{\partial}{\partial t}\tilde{\rho}_{1,2}^{(\nu)}(\mathbf{k}) &= -\bigl[\xi_\nu(\mathbf{k}-\mathbf{p}_{\mathrm{S}}/2)+\xi_\nu(\mathbf{k}+\mathbf{p}_{\mathrm{S}}/2)+2\bigl(\mu_{\mathrm{eff}}+\mu_{\mathrm{F}}^{\nu}\bigr)\bigr]\tilde{\rho}_{1,2}^{(\nu)}(\mathbf{k})\\
&\quad+|\Delta_\nu|e^{-\mathrm{i}\,\delta\theta_\nu}\bigl[\tilde{\rho}_{2,2}^{(\nu)}(\mathbf{k}-\mathbf{p}_{\mathrm{S}}/2)-\tilde{\rho}_{1,1}^{(\nu)}(\mathbf{k}+\mathbf{p}_{\mathrm{S}}/2)\bigr],
\end{aligned}
\tag{B20}
$$

with

$$
\begin{aligned}
\mathbf{p}_{\mathrm{S}} &\equiv \mathbf{p}_{\mathrm{S}}^{\nu}=-2\,e\,\mathbf{A},\quad \mu_{\mathrm{eff}}=e\,\phi+\frac{1}{2}\frac{\partial}{\partial t}\theta_{\nu_0},\\
\delta\theta_\nu &= \theta_{\nu_0}-\theta_\nu,\;|\Delta_\nu|=-e^{-\mathrm{i}\,\delta\theta_\nu}\sum_{\lambda,\mathbf{k}}g_{\nu,\lambda}\tilde{\rho}_{2,1}^{(\lambda)}(\mathbf{k}),\\
\mu_{\mathrm{F}}^{\nu} &\equiv \frac{1}{2}\bigl(\mu_{\mathrm{F}}^{\downarrow,\nu}+\mu_{\mathrm{F}}^{\uparrow,\nu}\bigr)=-g_{\nu,\nu}\sum_{\mathbf{k}}\bigl[1+\tilde{\rho}_{1,1}^{(\nu)}(\mathbf{k})-\tilde{\rho}_{2,2}^{(\nu)}(\mathbf{k})\bigr].
\end{aligned}
\tag{B21}
$$

The equations of motion of superfluid momentum $\mathbf{p}_S$ simplify to $\frac{\partial}{\partial t}\mathbf{p}_S = 2e\,\mathbf{E}$, while the SC order-parameter phase θ_{ν_0} is given by

$$\frac{\partial}{\partial t}\theta_{\nu_0} = -2\,e\,\phi + \frac{1}{2|\Delta_{\nu_0}|}\sum_{\nu,\mathbf{k}} g_{\nu_0,\nu}\big[\xi_\nu(\mathbf{k}-\mathbf{p}_S/2) + \xi_\nu(\mathbf{k}+\mathbf{p}_S/2) + 2\mu_F^\nu\big]\big(\tilde{\rho}_{1,2}^{(\nu)}(\mathbf{k}) + \tilde{\rho}_{2,1}^{(\nu)}(\mathbf{k})\big)$$

$$+ \frac{1}{|\Delta_{\nu_0}|}\sum_{\nu,\mathbf{k}} g_{\nu_0,\nu}|\Delta_\nu|\big[\tilde{\rho}_{1,1}^{(\nu)}(\mathbf{k}) - \tilde{\rho}_{2,2}^{(\nu)}(\mathbf{k})\big]\cos(\delta\theta_\nu). \tag{B22}$$

The above homogeneous equations of motion are equivalent to the conventional pseudospin model. To demonstrate this, we introduce the pseudospin

$$\sigma_0^{(\nu)}(\mathbf{k}) \equiv \frac{1}{2}\Big[\tilde{\rho}_{1,1}^{(\nu)}\Big(\mathbf{k}+\frac{\mathbf{p}_S}{2}\Big) + \tilde{\rho}_{2,2}^{(\nu)}\Big(\mathbf{k}-\frac{\mathbf{p}_S}{2}\Big)\Big],$$

$$\sigma_1^{(\nu)}(\mathbf{k}) \equiv \frac{1}{2}\Big[\tilde{\rho}_{1,2}^{(\nu)}(\mathbf{k})e^{i\theta_{\nu_0}} + \tilde{\rho}_{2,1}^{(\nu)}(\mathbf{k})e^{-i\theta_{\nu_0}}\Big],$$

$$\sigma_2^{(\nu)}(\mathbf{k}) \equiv \frac{1}{2i}\Big[\tilde{\rho}_{1,2}^{(\nu)}(\mathbf{k})e^{i\theta_{\nu_0}} - \tilde{\rho}_{2,1}^{(\nu)}(\mathbf{k})e^{-i\theta_{\nu_0}}\Big],$$

$$\sigma_3^{(\nu)}(\mathbf{k}) \equiv \frac{1}{2}\Big[\tilde{\rho}_{1,1}^{(\nu)}\Big(\mathbf{k}+\frac{\mathbf{p}_S}{2}\Big) - \tilde{\rho}_{2,2}^{(\nu)}\Big(\mathbf{k}-\frac{\mathbf{p}_S}{2}\Big)\Big], \tag{B23}$$

such that Eq. (B20) transforms to the Bloch equations of the conventional pseudospin model

$$\frac{\partial}{\partial t}\sigma_0^{(\nu)}(\mathbf{k}) = 0,$$

$$\frac{\partial}{\partial t}\sigma^{(\nu)}(\mathbf{k}) = 2\mathbf{b}^{(\nu)}(\mathbf{k}) \times \sigma^{(\nu)}(\mathbf{k}).$$

Here, $\sigma^{(\nu)}(\mathbf{k}) = (\sigma_1^{(\nu)}(\mathbf{k}), \sigma_2^{(\nu)}(\mathbf{k}), \sigma_3^{(\nu)}(\mathbf{k}))$ is the Anderson pseudospin, and $\mathbf{b}^{(\nu)}(\mathbf{k}) = (-\mathrm{Re}\Delta_\nu, \mathrm{Im}\Delta_\nu, [\xi_\nu(\mathbf{k}_-) + \xi_\nu(\mathbf{k}_+)]/2 + e\phi + \mu_F^\nu)$ is the pseudomagnetic field. Using $\sigma_i^{(\nu)}(\mathbf{k})$, the SC order parameter and the current density become

$$\Delta_\nu = -\sum_{\lambda,\mathbf{k}} g_{\nu,\lambda}\big[\sigma_x^{(\lambda)}(\mathbf{k}) - i\sigma_y^{(\lambda)}(\mathbf{k})\big],$$

$$J = \frac{e}{V}\sum_{\lambda,\mathbf{k}}\big\{\sigma_0^{(\lambda)}(\mathbf{k})\nabla_{\mathbf{k}}[\xi_\lambda(\mathbf{k}_+) + \xi_\lambda(\mathbf{k}_-)]$$

$$+ \sigma_3^{(\lambda)}(\mathbf{k})\nabla_{\mathbf{k}}[\xi_\lambda(\mathbf{k}_+) - \xi_\lambda(\mathbf{k}_-)]\big\},$$

respectively.

APPENDIX C: PHASE COHERENT PUMP-PROBE SPECTRA

So far, we have discussed contributions arising from excitations by one pulse that are sensed by the other. In this Appendix, we briefly discuss the wave-mixing signals in the THz-MDCS spectra that are generated by interference of *both* pump and probe excitations. As shown in Ref. [10], these signals show up in the THz-MDCS for weak excitation, where pulse A (B) can be considered as the probe of the nonequilibrium state driven by pulse B (A). Reference [10] showed that interference between pump and probe excitations dominates the THz-MDCS spectral features then, leading to correlated wave-mixing peaks. Unlike for the narrow-band strong pump and broadband weak probe excitation protocol used there,

here we consider two identical pulses that are both strong and broadband, so our results here relate to the results there only for weak pulse-pair fields. We can then decompose the density matrix driven by both pulses (pulse pair) as

$$\tilde{\rho}^{AB}(\mathbf{k}) = \tilde{\rho}^{A(B)}(\mathbf{k}) + \delta\tilde{\rho}^{B(A)}(\mathbf{k}), \tag{C1}$$

where $\delta\tilde{\rho}^{B(A)}$ describes the small probe-induced change in the density matrix of the nonequilibrium state driven by pulse A (B). The nonlinear signal is then determined by the equation of motion obtained by linearizing in terms of the probe but not the pump [10]:

$$\partial_t\delta\tilde{\rho}_0^B(\mathbf{k}) = -e\,\mathbf{E}_A \cdot \nabla_{\mathbf{k}}\,\delta\tilde{\rho}_3^{(\nu),B}(\mathbf{k}) - e\,\mathbf{E}_B \cdot \nabla_{\mathbf{k}}\,\tilde{\rho}_3^{(\nu),A}(\mathbf{k})$$

$$+ |\Delta_\nu^A|\delta\mathbf{p}_S^B \cdot \nabla_{\mathbf{k}}\Delta\tilde{\rho}_2^{(\nu),A}(\mathbf{k})$$

$$+ |\Delta_\nu^A|\Delta\theta_\nu^A\delta\mathbf{p}_S^B \cdot \nabla_{\mathbf{k}}\tilde{\rho}_1^{(\nu),A}(\mathbf{k})$$

$$+ |\Delta_\nu^A|\mathbf{p}_S^A \cdot \nabla_{\mathbf{k}}\delta\tilde{\rho}_2^{(\nu),B}(\mathbf{k})$$

$$+ |\Delta_\nu^A|\Delta\theta_\nu^A\mathbf{p}_S^A \cdot \nabla_{\mathbf{k}}\delta\tilde{\rho}_1^{(\nu),B}(\mathbf{k})$$

$$+ \delta|\Delta_\nu^B|\Delta\theta_\nu^A\mathbf{p}_S^A \cdot \nabla_{\mathbf{k}}\tilde{\rho}_1^{(\nu),A}(\mathbf{k})$$

$$+ \delta|\Delta_\nu^B|\mathbf{p}_S^A \cdot \nabla_{\mathbf{k}}\Delta\tilde{\rho}_2^{(\nu),A}(\mathbf{k})$$

$$+ O(\mathbf{p}_A^2) + O[(\Delta\theta_\nu)^2] + O(\mathbf{E}_B^2). \tag{C2}$$

Here, we expanded the equation of motion to first order in $\mathbf{p}_S$ and $\Delta\theta_\nu$ and neglected all orders of $O(\mathbf{E}_B^2)$. Of importance in this case is the coherent pump-probe modulation of the SC order-parameter amplitude by *both* pulses. Such pump-probe order-parameter modulation is controlled by the relative phase of the two fields through the time delay τ and should to be contrasted to the order-parameter quantum quench by a single pulse that dominates the signals here. The coherent pump-probe modulation of the order parameter is given by $\delta|\Delta_\nu^B| = |\Delta_\nu^{AB}| - |\Delta_\nu^A|$, while the probe-induced change of the superfluid momentum is given by $\delta\mathbf{p}_S^B = \mathbf{p}_S^{AB} - \mathbf{p}_S^A$. The equation of motion for $\partial_t\delta\tilde{\rho}_0^A(\mathbf{k})$ is obtained by exchanging the labels A and B in Eq. (C2). As demonstrated in Ref. [11], the terms in the first line of Eq. (C2) mainly drive the inversion-symmetry breaking. The second line of Eq. (C2) yields the pump-probe signal calculated in Ref. [18]. It only contributes to the nonlinear response when the probe pulse arrives after the pump pulse, such that is does not rely on the temporal overlap between both pulses. The corresponding signals show up as harmonic sidebands determined by Higgs and Leggett mode frequencies in the THz-MDCS spectra as demonstrated in Secs. IV A and IV B. In contrast to that, the contributions of lines three and four on the right-hand side of Eq. (C2) become significant when *pump and probe excitations overlap in time*. The conventional third-order

nonlinear processes and fifth-order Raman processes discussed in Secs. IV A and IV B are mainly generated by the third line on the right-hand side of Eq. (C2) [10]. These signals are determined by the equations of motion for $\delta \tilde{\rho}_2^{(\nu),B}(\mathbf{k})$, obtained by linearizing Eq. (21) with respect to the probe field:

$$
\begin{aligned}
\partial_t^2 \, \delta\tilde{\rho}_2^{(\nu),B}(\mathbf{k}) &+ \Big\{ \big[E_\nu^A(\mathbf{k})\big]^2 + 4\big|\Delta_\nu^A\big|^2 \cos^2 \Delta\theta_\nu^A \Big\} \delta\tilde{\rho}_2^{(\nu),B}(\mathbf{k}) \\
&+ \Big[-\partial_t E_\nu^A(\mathbf{k}) + 2\big|\Delta_\nu^A\big|^2 \sin 2\Delta\theta_\nu^A \Big] \delta\tilde{\rho}_1^{(\nu),B}(\mathbf{k}) \\
&= \delta S_\nu^{(2),B}(\mathbf{k}) - \delta\big[E_\nu^2(\mathbf{k})\big]\, \Delta\tilde{\rho}_2^{(\nu),A}(\mathbf{k}) \\
&\quad + \partial_t \delta[E_\nu(\mathbf{k})]\, \Delta\tilde{\rho}_1^{(\nu),A}(\mathbf{k}) \\
&\quad - \delta[\partial_t \delta\Delta_\nu' + \delta\Delta_\nu'' E_\nu(\mathbf{k})]\, N_\nu^A(\mathbf{k}) \\
&\quad - \big[\partial_t \delta\Delta_\nu'^{,A} + \delta\Delta_\nu''^{,A} E_\nu^A(\mathbf{k})\big]\, \delta[N_\nu(\mathbf{k})] \\
&\quad - 8\,\delta\Delta_\nu'^{,B} \Delta_\nu'^{,A}\, \Delta\tilde{\rho}_2^{(\nu),A}(\mathbf{k}) \\
&\quad - 4\Delta_\nu'^{,A} \delta\Delta_\nu''^{,B}\, \Delta\tilde{\rho}_1^{(\nu),A}(\mathbf{k}) - 4\Delta_\nu''^{,A} \delta\Delta_\nu'^{,B}\, \Delta\tilde{\rho}_1^{(\nu),A}(\mathbf{k}),
\end{aligned}
$$
(C3)

where the probe-induced changes are denoted by $\delta[\ldots]$. In particular, the pump–probe modulation of the SC order-parameter amplitude and phase are defined by

$$
\delta\Delta_\nu'^{,B} = \Delta_\nu'^{,AB} - \Delta_\nu'^{,A}, \quad \delta\Delta_\nu''^{,B} = \Delta_\nu''^{,AB} - \Delta_\nu''^{,A}. \quad \text{(C4)}
$$

The first term on the right-hand side of Eq. (C3), $\delta S_\nu^{(2),B}(\mathbf{k}) = S_\nu^{(2),AB}(\mathbf{k}) - S_\nu^{(2),A}(\mathbf{k})$, leads to pump-probe, four-wave-mixing, and third-harmonic generation signals which are generated by third-order nonlinear processes [10]. The dominant contribution of this term is

$$
\begin{aligned}
\delta\delta S_\nu^{(2),B}(\mathbf{k}) &\approx \tilde{\rho}_1^{(\nu),0}(\mathbf{k}) \big[(e\,\mathbf{E}_A \cdot \nabla_\mathbf{k})\big(\mathbf{p}_S^B \cdot \nabla_\mathbf{k}\big) \\
&\quad + (e\,\mathbf{E}_B \cdot \nabla_\mathbf{k})\big(\mathbf{p}_S^A \cdot \nabla_\mathbf{k}\big)\big]\xi_\nu(\mathbf{k}),
\end{aligned}
$$
(C5)

which drive the pseudospin oscillators via the sum- and difference-frequency Raman process $\omega_A \pm \omega_B = (\omega_0 \pm \omega_0, \mp\omega_0)$. Based on the fifth term on the right-hand side of

Eq. (C2), these processes lead to peaks at $\omega_A \pm \omega_B + \omega_A$ and $\omega_A \pm \omega_B - \omega_A$ in the THz-MDCS spectra. In particular, a pump-probe and four-wave-mixing signals are observable at $(\omega_0, -\omega_0)$ and (ω_0, ω_0), respectively, while a third-harmonic generation peak emerges at $(3\omega_0, -\omega_0)$. Exchanging pulses A and B results in pump-probe, four-wave-mixing, and third-harmonic generation signals at $(\omega_0, 0)$, $(\omega_0, -2\omega_0)$, and $(3\omega_0, -2\omega_0)$, respectively. These signals are observable in the THz-MDCS spectra in the perturbative excitation regime, where the nonlinear response can be described by susceptibility expansion.

The second and third terms on the right-hand side of Eq. (C3) describe fifth-order difference-frequency Raman processes which only slightly contribute to the THz-MDCS spectra [10]. Probe-induced changes of collective modes and charge fluctuations are described by the second and third lines on the right-hand side of Eq. (C3). The fourth and fifth lines of Eq. (C3) generate strong seventh-order correlated wave-mixing peaks when the system is excited with a strong narrow-band pump pulse and sensed by a weak broadband probe pulse as discussed in Ref. [10]. In particular, pseudospin oscillators at different momenta $\mathbf{k}$ are parametrically driven by the time-dependent modulation of the order parameter $\delta|\Delta_{A(B),h}| = |\Delta_{AB,h}| - |\Delta_{A(B),h}|$. This parametric driving leads to distinct high-order nonlinear peaks displaced from the conventional pump-probe peaks along the vertical ω_τ axis. In the case of narrow-band strong pump and weak broadband probe used in Ref. [10], the THz-MDCS spectra show four strong peaks which dominate over conventional third-order nonlinear signals and are generated by at least seventh-order nonlinear processes. Correlated pump-probe, four-wave-mixing, and third-harmonic generation peaks separate from the corresponding third-order nonlinear signals while a fourth strong correlated wave-mixing peak emerges in a spectral region far separated from the conventional signals. These contributions are negligible in the pulse-pair excitation scheme with two strong broad pulses studied in this paper.

[1] W. Kuehn, K. Reimann, M. Woerner, and T. Elsaesser, Phase-resolved two-dimensional spectroscopy based on collinear n-wave mixing in the ultrafast time domain, J. Chem. Phys. **130**, 164503 (2009).

[2] T. Maag, A. Bayer, S. Baierl, M. Hohenleutner, T. Korn, C. Schüller, D. Schuh, D. Bougeard, C. Lange, R. Huber, M. Mootz, J. E. Sipe, S. W. Koch, and M. Kira, Coherent cyclotron motion beyond Kohn's theorem, Nat. Phys. **12**, 119 (2016).

[3] F. Junginger, B. Mayer, C. Schmidt, O. Schubert, S. Mährlein, A. Leitenstorfer, R. Huber, and A. Pashkin, Nonperturbative interband response of a bulk InSb semiconductor driven off resonantly by terahertz electromagnetic few-cycle pulses, Phys. Rev. Lett. **109**, 147403 (2012).

[4] A. T. Tarekegne, K. J. Kaltenecker, P. Klarskov, K. Iwaszczuk, W. Lu, H. Ou, K. Norrman, and P. U. Jepsen, Subcycle nonlinear response of doped 4H silicon carbide revealed by two-dimensional terahertz spectroscopy, ACS Photon. **7**, 221 (2020).

[5] S. Pal, N. Strkalj, C.-J. Yang, M. C. Weber, M. Trassin, M. Woerner, and M. Fiebig, Origin of terahertz soft-mode nonlinearities in ferroelectric perovskites, Phys. Rev. X **11**, 021023 (2021).

[6] F. D. Fuller and J. P. Ogilvie, Experimental implementations of two-dimensional fourier transform electronic spectroscopy, Annu. Rev. Phys. Chem. **66**, 667 (2015).

[7] J. Lu, X. Li, H. Y. Hwang, B. K. Ofori-Okai, T. Kurihara, T. Suemoto, and K. A. Nelson, Coherent two-dimensional terahertz magnetic resonance spectroscopy of collective spin waves, Phys. Rev. Lett. **118**, 207204 (2017).

[8] C. L. Johnson, B. E. Knighton, and J. A. Johnson, Distinguishing nonlinear terahertz excitation pathways with two-dimensional spectroscopy, Phys. Rev. Lett. **122**, 073901 (2019).

[9] T. G. H. Blank, K. A. Grishunin, K. A. Zvezdin, N. T. Hai, J. C. Wu, S.-H. Su, J.-C. A. Huang, A. K. Zvezdin, and A. V. Kimel, Two-dimensional terahertz spectroscopy of nonlinear phononics in the topological insulator MnBi$_2$Te$_4$, Phys. Rev. Lett. **131**, 026902 (2023).

[10] M. Mootz, L. Luo, J. Wang, and l. E. Perakis, Visualization and quantum control of light-accelerated condensates by terahertz multi-dimensional coherent spectroscopy, Commun. Phys. **5**, 47 (2022).

[11] L. Luo, M. Mootz, J. H. Kang, C. Huang, K. Eom, J. W. Lee, C. Vaswani, Y. G. Collantes, E. E. Hellstrom, I. E. Perakis, C. B. Eom, and J. Wang, Quantum coherence tomography of light-controlled superconductivity, Nat. Phys. **19**, 1841 (2023).

[12] M. Puviani, R. Haenel, and D. Manske, Quench-drive spectroscopy and high-harmonic generation in BCS superconductors, Phys. Rev. B **107**, 094501 (2023).

[13] B. Cheng, D. Cheng, K. Lee, M. Mootz, C. Huang, L. Luo, Z. Chen, Y. Lee, B. Y. Wang, I. E. Perakis, Z.-X. Shen, H. Y. Hwang, and J. Wang, Evidence for highly damped Higgs mode in infinite-layer nickelates, arXiv:2310.02589.

[14] R. Matsunaga, N. Tsuji, H. Fujita, A. Sugioka, K. Makise, Y. Uzawa, H. Terai, Z. Wang, H. Aoki, and R. Shimano, Light-induced collective pseudospin precession resonating with Higgs mode in a superconductor, Science **345**, 1145 (2014).

[15] R. Matsunaga, N. Tsuji, K. Makise, H. Terai, H. Aoki, and R. Shimano, Polarization-resolved terahertz third-harmonic generation in a single-crystal superconductor NbN: Dominance of the Higgs mode beyond the BCS approximation, Phys. Rev. B **96**, 020505(R) (2017).

[16] F. Giorgianni, T. Cea, C. Vicario, C. P. Hauri, W. K. Withanage, X. Xi, and L. Benfatto, Leggett mode controlled by light pulses, Nat. Phys. **15**, 341 (2019).

[17] H. Chu, M.-J. Kim, K. Katsumi, S. Kovalev, R. D. Dawson, L. Schwarz, N. Yoshikawa, G. Kim, D. Putzky, Z. Z. Li, H. Raffy, S. Germanskiy, J.-C. Deinert, N. Awari, I. Ilyakov, B. Green, M. Chen, M. Bawatna, G. Cristiani, G. Logvenov *et al.*, Phase-resolved Higgs response in superconducting cuprates, Nat. Commun. **11**, 1793 (2020).

[18] C. Vaswani, J. H. Kang, M. Mootz, L. Luo, X. Yang, C. Sundahl, D. Cheng, C. Huang, R. H. J. Kim, Z. Liu, Y. G. Collantes, E. E. Hellstrom, I. E. Perakis, C. B. Eom, and J. Wang, Light quantum control of persisting Higgs modes in iron-based superconductors, Nat. Commun. **12**, 258 (2021).

[19] B. Cheng, D. Cheng, K. Lee, L. Luo, Z. Chen, Y. Lee, B. Y. Wang, M. Mootz, I. E. Perakis, Z.-X. Shen, H. Y. Hwang, and J. Wang, Evidence for d-wave superconductivity of infinite-layer nickelates from low-energy electrodynamics, Nat. Mater. (2024).

[20] N. Tsuji and H. Aoki, Theory of Anderson pseudospin resonance with Higgs mode in superconductors, Phys. Rev. B **92**, 064508 (2015).

[21] Y. Murotani, N. Tsuji, and H. Aoki, Theory of light-induced resonances with collective Higgs and Leggett modes in multiband superconductors, Phys. Rev. B **95**, 104503 (2017).

[22] M. Udina, T. Cea, and L. Benfatto, Theory of coherent-oscillations generation in terahertz pump-probe spectroscopy: From phonons to electronic collective modes, Phys. Rev. B **100**, 165131 (2019).

[23] M. Udina, J. Fiore, T. Cea, C. Castellani, G. Seibold, and L. Benfatto, Thz non-linear optical response in cuprates: predominance of the bcs response over the higgs mode, Faraday Discuss. **237**, 168 (2022).

[24] T. Papenkort, V. M. Axt, and T. Kuhn, Coherent dynamics and pump-probe spectra of BCS superconductors, Phys. Rev. B **76**, 224522 (2007).

[25] H. Krull, N. Bittner, G. Uhrig, D. Manske, and A. Schnyder, Coupling of Higgs and Leggett modes in non-equilibrium superconductors, Nat. Commun. **7**, 11921 (2016).

[26] Y.-Z. Chou, Y. Liao, and M. S. Foster, Twisting Anderson pseudospins with light: Quench dynamics in terahertz-pumped BCS superconductors, Phys. Rev. B **95**, 104507 (2017).

[27] L. Schwarz, B. Fauseweh, and N. E. A. Tsuji, Classification and characterization of nonequilibrium Higgs modes in unconventional superconductors, Nat. Commun. **11**, 287 (2020).

[28] M. Mootz, J. Wang, and I. E. Perakis, Lightwave terahertz quantum manipulation of nonequilibrium superconductor phases and their collective modes, Phys. Rev. B **102**, 054517 (2020).

[29] M. J. Stephen, Transport equations for superconductors, Phys. Rev. **139**, A197 (1965).

[30] T. Yu and M. W. Wu, Gauge-invariant theory of quasiparticle and condensate dynamics in response to terahertz optical pulses in superconducting semiconductor quantum wells. I. *s*-wave superconductivity in the weak spin-orbit coupling limit, Phys. Rev. B **96**, 155311 (2017).

[31] F. Yang and M. W. Wu, Gauge-invariant microscopic kinetic theory of superconductivity: Application to the optical response of Nambu-Goldstone and Higgs modes, Phys. Rev. B **100**, 104513 (2019).

[32] Y. Murotani and R. Shimano, Nonlinear optical response of collective modes in multiband superconductors assisted by nonmagnetic impurities, Phys. Rev. B **99**, 224510 (2019).

[33] G. Seibold, M. Udina, C. Castellani, and L. Benfatto, Third harmonic generation from collective modes in disordered superconductors, Phys. Rev. B **103**, 014512 (2021).

[34] L. Benfatto, C. Castellani, and G. Seibold, Linear and nonlinear current response in disordered *d*-wave superconductors, Phys. Rev. B **108**, 134508 (2023).

[35] X. Yang, C. Vaswani, C. Sundahl, M. Mootz, P. Gagel, L. Luo, J. Kang, P. Orth, I. Perakis, C. Eom *et al.*, Terahertz-light quantum tuning of a metastable emergent phase hidden by superconductivity, Nat. Mater. **17**, 586 (2018).

[36] X. Yang, C. Vaswani, C. Sundahl, M. Mootz, L. Luo, J. Kang, I. Perakis, C. Eom, and J. Wang, Lightwave-driven gapless superconductivity and forbidden quantum beats by terahertz symmetry breaking, Nat. Photonics **13**, 707 (2019).

[37] P. W. Anderson, Random-phase approximation in the theory of superconductivity, Phys. Rev. **112**, 1900 (1958).

[38] R. Sooryakumar and M. V. Klein, Raman scattering by superconducting-gap excitations and their coupling to charge-density waves, Phys. Rev. Lett. **45**, 660 (1980).

[39] P. B. Littlewood and C. M. Varma, Gauge-invariant theory of the dynamical interaction of charge density waves and superconductivity, Phys. Rev. Lett. **47**, 811 (1981).

[40] D. Podolsky, A. Auerbach, and D. P. Arovas, Visibility of the amplitude (Higgs) mode in condensed matter, Phys. Rev. B **84**, 174522 (2011).

[41] A. Moor, A. F. Volkov, and K. B. Efetov, Amplitude higgs mode and admittance in superconductors with a moving condensate, Phys. Rev. Lett. **118**, 047001 (2017).

[42] S. Nakamura, Y. Iida, Y. Murotani, R. Matsunaga, H. Terai, and R. Shimano, Infrared activation of the higgs mode by supercurrent injection in superconducting NbN, Phys. Rev. Lett. **122**, 257001 (2019).

[43] X. Yang, L. Luo, M. Mootz, A. Patz, S. L. Bud'ko, P. C. Canfield, I. E. Perakis, and J. Wang, Nonequilibrium pair breaking in Ba(Fe$_{1-x}$Co$_x$)$_2$As$_2$ superconductors: Evidence for formation of a photoinduced excitonic state, Phys. Rev. Lett. **121**, 267001 (2018).

[44] M. Puviani, L. Schwarz, X.-X. Zhang, S. Kaiser, and D. Manske, Current-assisted Raman activation of the Higgs mode in superconductors, Phys. Rev. B **101**, 220507(R) (2020).

[45] T. Cea, C. Castellani, and L. Benfatto, Nonlinear optical effects and third-harmonic generation in superconductors: Cooper pairs versus Higgs mode contribution, Phys. Rev. B **93**, 180507(R) (2016).

[46] C. Vaswani, M. Mootz, C. Sundahl, D. H. Mudiyanselage, J. H. Kang, X. Yang, D. Cheng, C. Huang, R. H. J. Kim, Z. Liu, L. Luo, I. E. Perakis, C. B. Eom, and J. Wang, Terahertz second-harmonic generation from lightwave acceleration of symmetry-breaking nonlinear supercurrents, Phys. Rev. Lett. **124**, 207003 (2020).

[47] Y. Nambu, Quasi-particles and gauge invariance in the theory of superconductivity, Phys. Rev. **117**, 648 (1960).

[48] C. Liu, T. Kondo, R. M. Fernandes, A. D. Palczewski, E. D. Mun, N. Ni, A. N. Thaler, A. Bostwick, E. Rotenberg, J. Schmalian, S. L. Bud'ko, P. C. Canfield, and A. Kaminski, Evidence for a Lifshitz transition in electron-doped iron arsenic superconductors at the onset of superconductivity, Nat. Phys. **6**, 419 (2010).

[49] R. M. Fernandes and J. Schmalian, Competing order and nature of the pairing state in the iron pnictides, Phys. Rev. B **82**, 014521 (2010).

[50] W. Kuehn, K. Reimann, M. Woerner, T. Elsaesser, and R. Hey, Two-dimensional terahertz correlation spectra of electronic excitations in semiconductor quantum wells, J. Phys. Chem. B **115**, 5448 (2011).

[51] G. Blumberg, A. Mialitsin, B. S. Dennis, M. V. Klein, N. D. Zhigadlo, and J. Karpinski, Observation of Leggett's collective mode in a multiband MgB$_2$ superconductor, Phys. Rev. Lett. **99**, 227002 (2007).

[52] M. V. Klein, Theory of raman scattering from Leggett's collective mode in a multiband superconductor: Application to MgB$_2$, Phys. Rev. B **82**, 014507 (2010).

[53] T. Cea and L. Benfatto, Signature of the Leggett mode in the A_{1g} Raman response: From MgB$_2$ to iron-based superconductors, Phys. Rev. B **94**, 064512 (2016).

[54] M. Ortolani, P. Dore, D. Di Castro, A. Perucchi, S. Lupi, V. Ferrando, M. Putti, I. Pallecchi, C. Ferdeghini, and X. X. Xi, Two-band parallel conductivity at terahertz frequencies in the superconducting state of MgB$_2$, Phys. Rev. B **77**, 100507(R) (2008).

[55] A. Patz, T. Li, S. Ran, R. M. Fernandes, J. Schmalian, S. L. Bud'ko, P. C. Canfield, I. E. Perakis, and J. Wang, Ultrafast observation of critical nematic fluctuations and giant magnetoelastic coupling in iron pnictides, Nat. Commun. **5**, 3229 (2014).

[56] A. Patz, T. Li, L. Luo, X. Yang, S. Bud'ko, P. C. Canfield, I. E. Perakis, and J. Wang, Critical speeding up of nonequilibrium electronic relaxation near nematic phase transition in unstrained Ba(Fe$_{1-x}$Co$_x$)$_2$As$_2$, Phys. Rev. B **95**, 165122 (2017).

[57] T. V. Shahbazyan, N. Primozich, I. E. Perakis, and D. S. Chemla, Femtosecond coherent dynamics of the fermi-edge singularity and exciton hybrid, Phys. Rev. Lett. **84**, 2006 (2000).

[58] P. C. Lingos, A. Patz, T. Li, G. D. Barmparis, A. Keliri, M. D. Kapetanakis, L. Li, J. Yan, J. Wang, and I. E. Perakis, Correlating quasiparticle excitations with quantum femtosecond magnetism in photoexcited nonequilibrium states of insulating antiferromagnetic manganites, Phys. Rev. B **95**, 224432 (2017).

[59] P. C. Lingos, M. D. Kapetanakis, J. Wang, and I. E. Perakis, Light-wave control of correlated materials using quantum magnetism during time-periodic modulation of coherent transport, Commun. Phys. **4**, 60 (2021).

[60] E. A. Yuzbashyan, O. Tsyplyatyev, and B. L. Altshuler, Relaxation and persistent oscillations of the order parameter in fermionic condensates, Phys. Rev. Lett. **96**, 097005 (2006).

[61] E. A. Yuzbashyan, Normal and anomalous solitons in the theory of dynamical Cooper pairing, Phys. Rev. B **78**, 184507 (2008).

[62] H. P. Ojeda Collado, J. Lorenzana, G. Usaj, and C. A. Balseiro, Population inversion and dynamical phase transitions in a driven superconductor, Phys. Rev. B **98**, 214519 (2018).

[63] L. Luo, D. Cheng, B. Song, L.-L. Wang, C. Vaswani, P. M. Lozano, G. Gu, C. Huang, R. H. J. Kim, Z. Liu, J.-M. Park, Y. Yao, K. Ho, I. E. Perakis, Q. Li, and J. Wang, A light-induced phononic symmetry switch and giant dissipationless topological photocurrent in ZrTe$_5$, Nat. Mater. **20**, 329 (2021).

[64] L. Luo, X. Yang, X. Liu, Z. Liu, C. Vaswani, D. Cheng, M. Mootz, X. Zhao, Y. Yao, C.-Z. Wang, K.-M. Ho, I. E. Perakis, M. Dobrowolska, J. K. Furdyna, and J. Wang, Ultrafast manipulation of topologically enhanced surface transport driven by mid-infrared and terahertz pulses in Bi$_2$Se$_3$, Nat. Commun. **10**, 607 (2019).

[65] X. Yang, L. Luo, C. Vaswani, X. Zhao, Y. Yao, D. Cheng, Z. Liu, R. H. J. Kim, X. Liu, M. Dobrowolska-Furdyna, J. K. Furdyna, I. E. Perakis, C. Wang, K. Ho, and J. Wang, Light control of surface–bulk coupling by terahertz vibrational coherence in a topological insulator, npj Quantum Mater. **5**, 13 (2020).

[66] B. Cheng, D. Cheng, T. Jiang, W. Xia, B. Song, M. Mootz, L. Luo, I. E. Perakis, Y. Yao, Y. Guo, and J. Wang, Chirality manipulation of ultrafast phase switchings in a correlated CDW-Weyl semimetal, arXiv:2308.03895.

[67] C. Vaswani, L.-L. Wang, D. H. Mudiyanselage, Q. Li, P. M. Lozano, G. D. Gu, D. Cheng, B. Song, L. Luo, R. H. J. Kim, C. Huang, Z. Liu, M. Mootz, I. E. Perakis, Y. Yao, K. M. Ho, and J. Wang, Light-driven raman coherence as a nonthermal route to ultrafast topology switching in a dirac semimetal, Phys. Rev. X **10**, 021013 (2020).

[68] A. Patz, T. Li, X. Liu, J. K. Furdyna, I. E. Perakis, and J. Wang, Ultrafast probes of nonequilibrium hole spin relaxation in the ferromagnetic semiconductor GaMnAs, Phys. Rev. B **91**, 155108 (2015).

[69] T. Li, A. Patz, L. Mouchliadis, J. Yan, T. A. Lograsso, I. E. Perakis, and J. Wang, Femtosecond switching of magnetism via strongly correlated spin–charge quantum excitations, Nature (London) **496**, 69 (2013).

[70] B. Q. Song, X. Yang, C. Sundahl, J.-H. Kang, M. Mootz, Y. Yao, I. E. Perakis, L. Luo, C. B. Eom, and J. Wang, Ultrafast martensitic phase transition driven by intense terahertz pulses, Ultrafast Sci. **3**, 0007 (2023).